Ceramics International xxx (xxxx) xxx

Contents lists available at ScienceDirect

Ceramics International

journal homepage: www.elsevier.com/locate/ceramint

In-situ ceramic formation in a (NbC–TiC–TiB_2) precursor-modified Inconel 718 via SPS and laser surface melting: Composite structure evolution and tribological performance

Yu.G. Chabak [a,b], V.G. Efremenko [a,b,*], N.P. Zaichuk [c], V. Puchý [a], B.V. Efremenko [b], I. Petrišinec [a], K. Kamyshnykova [d], I.I. Sili [b]

[a] Institute of Materials Research of Slovak Academy of Sciences, Kosice, Slovakia
[b] Pryazovskyi State Technical University, Dnipro, Ukraine
[c] Lutsk National Technical University, Lutsk, Ukraine
[d] Institute of Materials and Machine Mechanics of Slovak Academy of Sciences, Bratislava, Slovakia

ARTICLE INFO

Keywords:
Inconel 718
Spark plasma sintering
Laser surface melting
In-situ ceramics
Compositionally complex ceramics
Tribology

ABSTRACT

An Inconel 718-based composite reinforced with a multicomponent NbC-TiC-TiB_2 ceramic precursor (5-20 vol%) was fabricated via a dual-stage processing route combining spark plasma sintering and subsequent laser surface melting in air. This study investigated the structural and mechanical evolution of the composite through the *in-situ* alteration of the ceramic phase constitution. Under superheated molten pool conditions, complete dissolution of the precursor occurred, driving a non-equilibrium crystallization pathway. During primary crystallization, complex Ti-Al-O cores formed, followed by heterogeneous nucleation of multicomponent ceramic phases comprising faceted (Nb,Ti,Cr,Mo) (B,C) carboboride shells and a discontinuous interdendritic eutectic network of (Cr,Nb,Mo,Ti)B_2 borides. Progressive precursor addition increased the area fractions of equiaxed ceramic particles and eutectic boride inclusions to 3.3% and 18.0%, respectively, while promoting non-linear phase coarsening due to the expanded solidification window. This structural modification increased nanoindentation hardness by 36% (from 3.22 to 4.38 GPa) and modulus by 14% (from 200.4 to 228.7 GPa), while maintaining the indentation plasticity parameter at a comparable level. Tribological testing showed that increasing the precursor content drove a progressive reduction in friction coefficient from 0.95 to 0.77 and a 2.4-fold decrease in wear rate. SEM and EDS examinations of the wear tracks indicated a transition from severe adhesive and oxidative wear toward the formation of compact tribolayers and reduced material removal in the precursor-modified composites. These results demonstrate that the NbC-TiC-TiB_2 precursor substantially influences phase evolution during laser processing and improves the wear resistance of the resulting composite layers.

1. Introduction

Nickel-based superalloys, particularly Inconel 718 (IN718), are benchmark materials for high-temperature applications in the aerospace, marine, and power generation industries [1]. Their industrial utility stems from a balanced combination of high-temperature tensile strength, creep resistance, and oxidation stability. The mechanical hardening of IN718 is achieved through the coherent precipitation of γ'' (Ni_3Nb) and γ' ($Ni_3(Al,Ti)$) phases within a face-centered cubic (FCC) matrix [2]. These precipitates hinder dislocation motion, enabling the alloy to maintain its mechanical properties at service temperatures up to 650 °C [3]. However, the thermal demands of modern turbine engines increasingly approach or exceed the operational limits of monolithic IN718. At temperatures above 650-700 °C, the metastable γ'' phase coarsens or transforms into the stable but brittle δ phase, resulting in a substantial loss of strength. Additionally, IN718 exhibits limited wear resistance under high-load sliding and high-temperature erosion conditions [4]. To address these limitations, development has shifted toward particle-reinforced metal matrix composites (PMMCs), which incorporate hard ceramic phases to improve both thermal stability and tribological performance [5].

The performance of PMMCs is largely determined by the interfacial

* Corresponding author.Institute of Materials Research of Slovak Academy of Sciences, Kosice, Slovakia.
E-mail addresses: viefremenko@saske.sk, vgefremenko@gmail.com (V.G. Efremenko), ummskamy@savba.sk (K. Kamyshnykova).

https://doi.org/10.1016/j.ceramint.2026.10.401
Received 1 September 2026; Received in revised form 12 October 2026; Accepted 26 October 2026
Available online 28 October 2026
0272-8842/© 2026 Elsevier Ltd and Techna Group S.r.l. All rights are reserved, including those for text and data mining, AI training, and similar technologies.

bonding strength between the reinforcement and the matrix. In conventional *ex-situ* composites, the mechanical addition of particle often leads to poor wettability and premature debonding under stress. In contrast, *in-situ* synthesis utilizes internal chemical reactions to precipitate reinforcing phases during processing, resulting in thermodynamically stable, coherent or semi-coherent interfaces that enhance load transfer and prevent particle pull-out during wear [6]. *In-situ* reactions have successfully been used to form binary ceramic inclusions (TiC, (Nb, Ti)C, TiB_2, WC, TiCN, TiN) across various Al [7], Fe [8], Cu [9], and Ni-based systems [10–17], improving both hardness and thermal stability compared to their ex-situ counterparts. However, emerging thermal and mechanical demands require a shift toward compositionally complex, entropy-stabilized multicomponent phases capable of providing superior lattice distortion hardening and barrier-limited wear protection [18–20].

Traditional liquid-state processing of Ni-based PMMCs, such as stir casting or vacuum induction melting, often results in an inhomogeneous ceramic distribution due to density mismatches and poor wettability. It may also promote brittle eutectic formation, compromising fracture toughness [21]. Similarly, deposition methods [22,23] and surface modification techniques [24,25] are restricted to surface layers or specific geometries, while hot isostatic pressing is hindered by prolonged thermal cycles that promote grain growth [26]. To overcome the limitations of bulk melting and allow for precise phase management, powder metallurgy offers a controlled alternative. Among these techniques, spark plasma sintering (SPS) ensures near-theoretical densification through localized Joule heating at particle contacts under a pulsed direct current [27–29]. This rapid consolidation at lower temperatures preserves the fine-grained matrix and prevents the uncontrolled coarsening of ceramic particles. However, the solid-state nature of SPS often limits the extent of *in-situ* chemical transformations.

To trigger the formation of complex multicomponent phases, subsequent Laser Surface Melting (LSM) offers a potential solution. The high energy density of the laser beam induces localized melting followed by ultra-fast solidification (10^3-10^6 K/s) [17], forcing the system into an extreme nonequilibrium state [30]. This thermal cycle may facilitates the dissolution of primary ceramics within the superheated liquid nickel matrix and their re-precipitation as sub-micron or nanoscale *in-situ* phases with enhanced interfacial bonding and reinforcement potential [31,32]. In this framework, the initial ceramic particles act as precursors for the formation of new complex phases. A similar precursor approach, using Ti_2AlC MAX phases in an Inconel 718 matrix, successfully triggered the *in-situ* formation of ultrafine TiC particles [33], as well as a phase complex comprising (Nb,Ti) (C,N) and γ' [34], while completely suppressing the precipitation of the brittle Laves phase.

The selection of reinforcing phases represents a critical design decision in composite engineering. While monolithic ceramics like WC or TiC are widely studied [35,36], recent research has shifted toward complex, multicomponent systems that provide synergistic strengthening [37,38]. The combined use of different Nb, Ti, B-based precursors into the Inconel 718 matrix offers a route to in situ reinforcement. The chemical partitioning of these elements during high-energy processing drives the formation of complex carboborides that mechanically shield the matrix from wear. Concurrently, these phases can incorporate interstitial oxygen, which may originate from the powder precursors or processing environment, into their crystal lattice, promoting the protective self-renewing tribolayers during sliding [39]. Despite extensive research on Inconel composites, the specific *in-situ* evolution of the multicomponent Nb-Ti-B-C system during the transition from solid-state sintering to laser melting remains unexplored. Consequently, it remains unclear how the complete dissolution of primary ceramics in the melt pool influences phase composition, entropy-driven stabilization, and the resulting wear mechanisms.

This work aims to address this gap by systematically investigating the microstructural evolution of an Inconel 718-based PMMC reinforced with the NbC-TiC-TiB_2 precursor during hybrid SPS-laser processing. Using a comprehensive characterization methodology, we tracked phase transformation and chemical partitioning as the precursor particles evolved into integrated, entropy-stabilized multicomponent ceramic phases. Furthermore, nanoindentation and tribological testing were used to establish links between the processing mode, mechanical response, and wear mechanisms. The obtained results provide new insights into the design of advanced, wear-resistant composite systems.

2. Materials and methods

The composite was fabricated in two stages: spark plasma sintering followed by laser surface melting. The powder feedstock for sintering consisted of an IN718 matrix alloy (Fig. 1a) and a ceramic filler. The filler was prepared by blending NbC, TiC, and TiB_2 powders (Fig. 1b) in equal volume fractions (33.3 vol% each). These specific ceramic phases were selected for their high melting points (NbC: 3500-3600 °C, TiC: 3067-3150 °C, TiB_2: 2980-3230 °C), and hardness values (NbC: 19.6 GPa, TiC: 28-35 GPa, TiB_2: 34-40 GPa) [40–42]. Despite the strong atomic bonding implied by these properties, the thermal input from the laser was expected to cause complete dissolution of the fillers through contact melting. Upon cooling, the high enthalpy of formation of the ceramics was expected to promote the precipitation of ultra-fine reinforcing phases, serving as the nucleation sites for subsequent phase formation. Furthermore, the isostructural FCC nature of NbC and TiC should promote mutual solubility and strong bonding at the matrix–inclusion interface.

The particle sizes of the IN718 and the ceramic filler ranged from 7 to 44 μm (average 23.7 ± 2.9 μm) and from 0.6 to 5.3 μm (average 3.63 ± 0.15 μm), respectively (Fig. 1c). Several variants of the IN718–ceramic composites were fabricated with ceramic volume fractions of 5, 10, and 20 vol% (Fig. 1d-f), along with a ceramic-free IN718 alloy prepared as a reference. The resulting samples were designated as IN-0 (ceramic-free), IN-5, IN-10, and IN-20, respectively. The powder feedstock was prepared using a TURBULA® three-dimensional shaker mixer with a total mixing time of 4 h for both the pure ceramic filler and the final IN718–ceramic compositions.

To establish a precise baseline for subsequent calculations, the chemical composition of the reference ceramic-free IN718 alloy (IN-0) was experimentally verified after SPS using an optical emission spectrometer (NCS Labspark 1000). The analysis yielded the following concentrations (wt.%): 52.45 Ni, 19.01 Cr, 18.22 Fe, 5.42 Nb, 2.93 Mo, 0.89 Ti, 0.47 Al, 0.30 Si, 0.27 Co, and 0.04C, confirming its compliance with ASTM B637. Based on these data, the elemental weight fractions for the IN718–ceramic mixtures were calculated and are presented in Table 1. As the ceramic volume fraction increased, the total niobium content in the mixture nearly doubled relative to the pristine IN718 matrix (reaching 10.45 wt%), while the titanium content increased almost sevenfold (up to 6.88 wt%). Concurrently, the carbon and boron weight fractions rose systematically to 1.65 wt% and 1.22 wt%, respectively.

The prepared powder mixtures were consolidated into discs (30 mm in diameter, 5 mm in thickness) using an HP D 10SD (FCT Systeme) spark plasma sintering system. The fabrication parameters included a vacuum of 5 Pa, a heating rate of 100 K/min, a peak temperature of 1000 °C with a 10 min dwell time, and a maximum axial pressure of 50 MPa. The resulting discs were designated as SPS samples. Their density was determined via the Archimedes method using a Radwag Kit-85 system (Radwag). The porosity area fraction was calculated in the microstructure images using ImageJ software.

Subsequent laser surface melting was applied to promote the dissolution and *in-situ* reaction of the powder constituents within the melt pool, resulting in solidification into a multi-phase structure. Following the SPS stage, the flat surface of the disc underwent laser surface melting in ambient air using a 1064 nm fiber laser on a TruFiber 400 station (TRUMPF). The operational parameters were set as follows: laser power of 400 W, scanning speed of 5 mm/s, beam diameter of 1.3 mm, focal

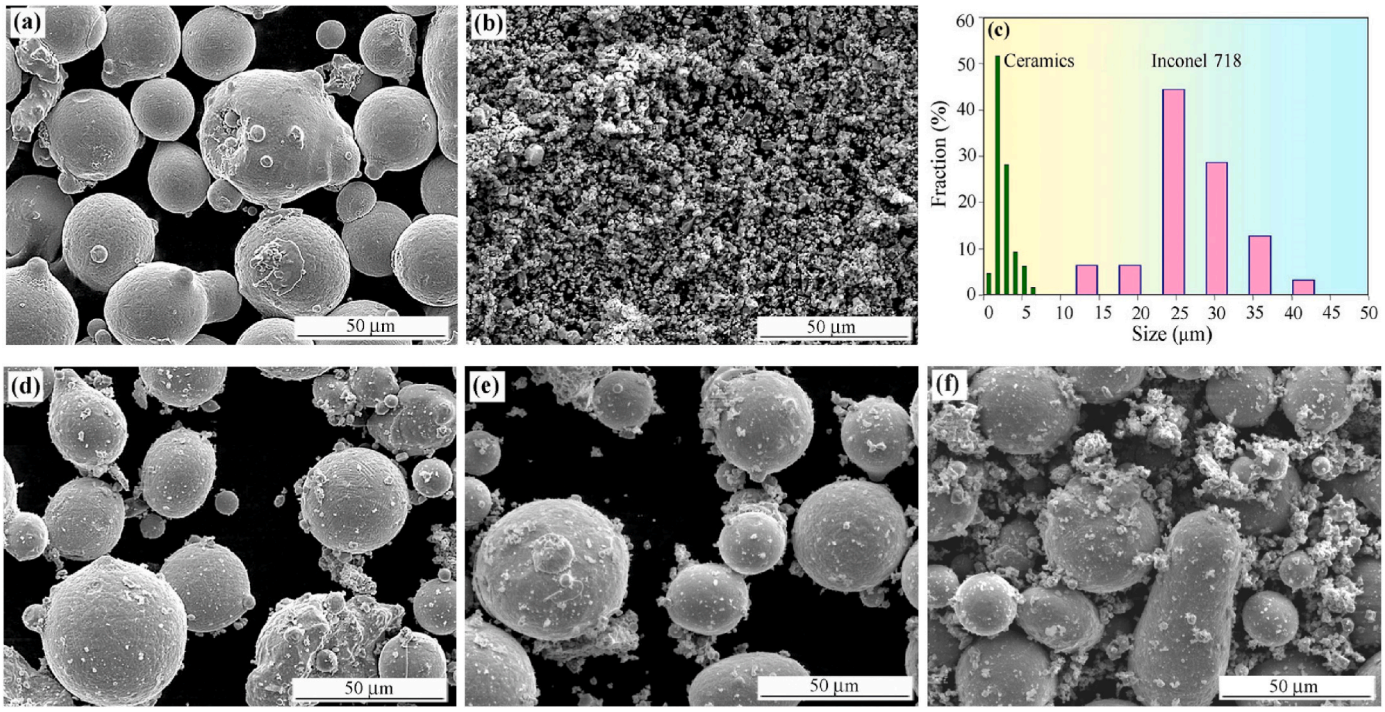

Fig. 1. SEM micrographs of the starting powders: (a) Inconel 718 and (b) mixed ceramics; (c) particle-size distributions of the IN718 and mixed ceramic powders; and SEM micrographs of the powder mixtures with a ceramic volume fraction of (d) 5%, (e) 10%, and (f) 20%.

Table 1
Measured chemical compositions (wt.%) of the sintered IN-0 reference alloy and calculated elemental concentrations of the IN718–ceramic mixtures.

Ceramic fraction, vol% (alloy designation)	Ni	Cr	Nb	Mo	Ti	Al	Si	Co	C	B	Fe
0 (IN-0)	52.45	19.01	5.42	2.93	0.89	0.47	0.30	0.27	0.04	–	18.22
5 (IN-5)	50.60	18.34	6.62	2.83	2.32	0.45	0.29	0.26	0.42	0.29	17.58
10 (IN-10)	48.70	17.65	7.86	2.72	3.79	0.44	0.28	0.25	0.82	0.59	16.90
20 (IN-20)	44.70	16.20	10.45	2.50	6.88	0.40	0.26	0.23	1.65	1.22	15.51

length of 20 mm, and 30% track overlap. These specific processing conditions were adapted from literature data on the LSM of 3D-printed Ni-based superalloys [43] to ensure sufficient energy density for the complete surface melting of the SPS specimens. The treatment was conducted without shielding gas to allow interaction between the molten pool and atmospheric oxygen.

The cross-sectional microstructure of the laser-modified layer was examined after grinding with SiC papers and final mirror polishing with a 0.25 μm diamond paste. Chemical etching was performed using a freshly prepared aqua regia solution consisting of concentrated HNO_3 and HCl, which was subsequently diluted with distilled H_2O (30 vol% relative to the aqua regia volume) to ensure controlled contrast between the matrix and the *in-situ* ceramic precipitates. Structural evaluation was carried out via a JSM-7000F (JEOL) and JSM-IT810 (JEOL) scanning electron microscopes (SEMs). Phase chemistry and elemental mapping were evaluated through energy-dispersive X-ray spectroscopy (EDS) with an INCAx-sight detector (Oxford Instruments) and electron probe microanalysis (EPMA) on a Field-Emission EPMA-8050G (Shimadzu) system. The chemical composition of each phase was determined based on EDS spectra collected from at least 10 different points in each phase across at least three distinct areas, followed by averaging the results. Phase identification was performed using an X'Pert PRO (PANalytical) diffractometer (Co-Kα source, 40 kV, 50 mA, 0.03342° step size, 0.0689°/s scan speed). The equilibrium solidification path was thermodynamically simulated using the JMatPro® software package.

The micromechanical behavior was investigated by nanoindentation testing on a G200 Nano Indenter (Agilent). Each indent was made at a constant displacement rate of 10 nm/s to a maximum load of 500 mN. Statistical accuracy was achieved by mapping a 10 × 10 indentation matrix with an interval of 50 μm between individual points, after which the data were averaged. In addition to the standard indentation hardness and indentation modulus, additional energy-based metrics were derived from the experimental load-displacement curves according to ISO 14577-1 via the procedure described in Ref. [44]. Specifically, the elastic recovery index (ERI) and plasticity index (PI) were assessed by dividing the total indentation work (W_t) into elastic (W_e) and plastic (W_p) constituents:

$$ERI = \frac{W_e}{W_t} \quad (1)$$

$$PI = \frac{W_p}{W_t} \quad (2)$$

Moreover, the h_p/h_{max} ratio was adopted to evaluate the fraction of residual plastic deformation relative to the peak penetration depth [45].

To quantitatively evaluate the non-equilibrium solidification parameters and the local cooling rate during LSM, the primary dendrite arm spacing (*PDAS*) of the IN718 matrix was determined using the SEM micrographs. Statistical reliability was achieved through multi-point linear intercept profiling conducted across 4-5 independent micrographs for each investigated material configuration. The collected *PDAS* data were subsequently used to calculate the local cooling rate within the laser melt pool utilizing a Kurz–Fisher solidification relationship [46] empirically modified for the laser-engineered net shaping process

configurations [47]:

$$PDAS = 1100 \cdot (\dot{T})^{-0.65}, \quad (3)$$

where *PDAS* is the primary dendrite arm spacing (μm), $\dot{T}$ is the local cooling rate (K/s), and the pre-exponential scaling factor and exponent are adapted from Ref. [47], with the scaling factor expressed in μm·(K/s)$^{0.65}$.

Tribological performance under sliding wear conditions was evaluated using a Micron-tribo (Micron System) tribometer [48] in a reciprocating ball-on-plate configuration. Prior to testing, specimen surfaces were mirror-polished to ensure accurate characterization of the wear track. A 3 mm cemented carbide ball was loaded against the surface under a constant normal force (F) of 1.96 N and subjected to 2000 reciprocating cycles at an amplitude of 4300 μm and a frequency of 2.5 Hz; the total sliding distance (L) was 17.2 m. The friction force was recorded at 10 Hz and converted into the coefficient of friction (CoF). Due to the inherent kinematics of reciprocating motion, the raw CoF profiles exhibited high-frequency transient noise and characteristic drops to zero at the displacement reversal positions (dead points). To eliminate this noise and these zero-value drops, raw datasets were post-processed by first taking the absolute values of the friction force and then applying a 150-point moving average filter to extract steady-state friction values [49]. The resulting values were averaged over the final 1000 cycles to define a steady-state friction coefficient. Worn surface topography was evaluated using a Micron-beta (Micron System) non-contact optical profilometer [50] over a track length of 1800 μm. These 3D data quantified the total wear track volume (V_{TR}), corresponding to the material displaced below the baseline, and the pile-up volume (V_P), corresponding to the material accumulated along the edges. The net material volume loss (ΔV) was calculated as $\Delta V = V_{TR}$

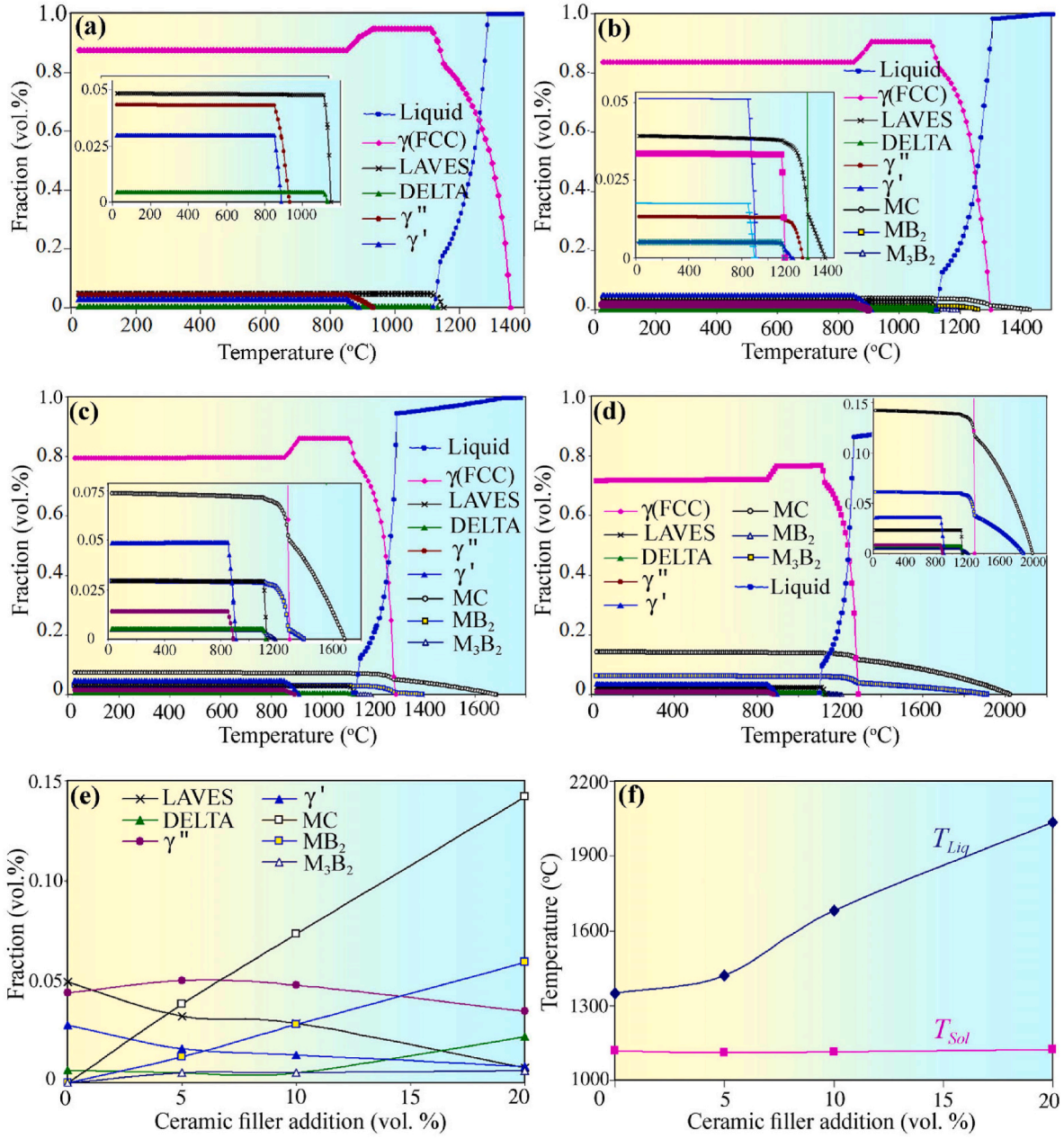

Fig. 2. Thermodynamic simulation of phase evolution in IN718–ceramic composites: equilibrium volume fractions of phases for (a) IN-0, (b) IN-5, (c) IN-10, and (d) IN-20; (e) effect of ceramic filler addition on the volume fraction of secondary phases at 25 °C; and (f) variation of the liquidus and solidus temperatures with ceramic filler volume fraction. Insets in (a-d) provide magnified views of the low-temperature regions of secondary-phase solidification.

– V_P. For statistical reliability, four tests were performed, and the results were averaged. The wear resistance was evaluated using the wear rate parameter:

$$WR = \frac{\Delta V}{F \cdot L}. \quad (4)$$

3. Results

3.1. Thermodynamic simulation of phase equilibrium in metal-ceramic composites

To theoretically assess the solidification path and phase evolution as a function of the NbC–TiC–TiB_2 precursor volume fraction, thermodynamic simulations were performed using the JMatPro® software package (Fig. 2). The calculations assumed that high-energy laser exposure induced the complete dissolution of the initial ceramic components into a homogeneous, supersaturated liquid phase within the melt pool.

Fig. 2a-d presents the computed temperature-dependent phase fraction diagrams for the investigated compositions (IN-0, IN-5, IN-10, and IN-20, respectively), illustrating the thermodynamic stability and dissolution–precipitation limits of individual phases over a wide temperature range. To provide a comprehensive comparative summary of these transformations at room temperature, the equilibrium volume fraction of secondary phases at 25 °C was extracted from these calculations and plotted in Fig. 2e. For the unreinforced IN718 matrix (IN-0), the predicted phase set aligns with conventional Ni-based superalloy metallurgy, where the main strengthening phases are the metastable γ″-Ni_3Nb (~5 vol%) and γ′-Ni_3(Al,Ti) (~2.8 vol%) intermetallics, accompanied by ~5 vol% of the Laves phase and ~0.5 vol% of the δ phase.

Introducing the ceramic precursor substantially alters the phase balance, increasing the volume fraction of MC-type carbides and MB_2/M_3B_2-type borides. The volume fraction of MC carbides increases linearly from 0% (IN-0) to ~14.5 vol% (IN-20) as the introduced carbon binds with titanium and niobium to form MC carbides. Simultaneously, the introduction of boron initiates the crystallization of refractory borides: the MB_2 phase (predominantly TiB_2-based) reaches ~6 vol% at 20 vol% precursor content, while the M_3B_2 phase peaks at ~2.4 vol% at ceramic precursor contents of 15-20 vol%.

Crucially, increasing the filler content to 20 vol% monotonically reduces the Laves phase to nearly zero. This indicates that the excess niobium is preferentially consumed in the formation of thermodynamically more stable *in-situ* MC carbides, thereby mitigating the formation of the brittle topologically close-packed (TCP) Laves phase. Concurrently, the γ″ fraction decreases to ~3.5 vol% in IN-20, whereas the γ′ phase exhibits an anomalous trend, decreasing to a minimum at 10 vol% ceramic precursor before rising sharply to ~2.2 vol% at 20 vol%. This behavior is governed by the complex partitioning of titanium among the emerging carbides, borides, and the FCC-γ nickel matrix. The fraction of the stable δ phase remains consistently low (within 1-2 vol%) across the entire concentration range.

Fig. 2f depicts the liquidus (T_{Liq}) and solidus (T_{Sol}) temperatures as a function of the ceramic volume fraction. For the baseline IN-0 alloy, T_L stands at ~1350 °C. A 5 vol% ceramic addition induces a minor shift to ~1420 °C, preserving conventional matrix melting behavior. However, higher filler concentrations lead to a sharp, stepwise rise in T_L, reaching ~1680 °C for IN-10 and an extreme value of ~2010 °C for IN-20. In contrast, T_S remains highly stable within the 1110-1125 °C range. This substantial widening of the solidification interval reflects the formation of a refractory quasi-eutectic melt, in which excess Ti, Nb, and B shifts the liquidus toward the primary crystallization of high-temperature borides and carbides directly from the liquid phase. This factor imposes strict constraints on the LSM parameters and requires sufficient volumetric energy input to maintain the melt pool above the critical liquidus temperature.

In summary, the thermodynamic analysis reveals that increasing the complex filler content from 0 to 20 vol% induces a substantial change in the predicted phase composition: conventional precipitation hardening by γ″ and γ′ is largely superseded by an *in-situ* framework reinforcement containing up to 23 vol% of high-temperature MC carbides and MB_2/M_3B_2 borides that form preferentially along interdendritic boundaries.

3.2. Microstructure characterization

3.2.1. Microstructure after spark plasma sintering

Fig. 3 shows the cross-sectional BSE (backscattered electron)-SEM micrographs of the IN718–(NbC, TiC, TiB_2) composites processed via SPS. The pure alloy (IN-0, Fig. 3a) exhibits a high degree of consolidation, with nearly complete elimination of the initial particle interfaces due to intensive mutual diffusion, resulting in a dense monolithic matrix with minimal isolated porosity (0.49% by area). Introducing 5 vol% of the ceramic filler (Fig. 3b) shifts the morphology toward a discrete network structure, where the high-melting phases preferentially localize along the superalloy grain boundaries. At higher concentrations of 10 vol% (Figs. 3c) and 20 vol% filler (Fig. 3d), the interparticle layers thicken monotonically, transforming into a continuous network that completely isolates the IN718 particles and blocks direct metallic grain-to-grain contact. In the BSE mode, these extended interparticle channels appear dark or black due to the low atomic numbers of boron (Z = 5) and carbon (Z = 6), visually resembling shrinkage porosity.

To resolve this methodology issue, EDS elemental mapping was employed (Fig. 4). The metallic matrix grains exhibit homogeneous concentrations of Ni, Fe, and Cr, with a sharp signal drop at the boundaries, confirming the barrier role of the ceramic network. Crucially, the spatial distribution of Nb, Ti, B, and C is strictly confined to these boundary regions. The bright angular inclusions are enriched in Nb and C, confirming the presence of dense NbC carbides. Most importantly, the geometry of the dark channels closely coincides with the continuous regions of maximum Ti, B, and C intensities. This conclusively demonstrates that the apparent interparticle porosity is actually filled with dense, lightweight refractory ceramics – TiB_2 (Z ≈ 10.6) and TiC (Z ≈ 14) – which possess a low backscattering coefficient. True porosity is merely residual and point-like, identified by the simultaneous absence of all metallic and ceramic signals. Thus, SPS at 1000 °C appears to produce a dense composite framework where the dark boundaries represent a tightly packed heterophase ceramic mixture rather than destructive voids, ensuring the structural integrity of the synthesized materials.

The physical density of the SPS-processed materials gradually decreases as the ceramic filler content increases, from 7.42 ± 0.003 g cm^{-3} for IN-0 to 7.35 ± 0.003 g cm^{-3} for IN-5, 7.05 ± 0.005 g cm^{-3} for IN-10, and 6.74 ± 0.004 g cm^{-3} for IN-20.

3.2.2. Microstructure after laser surface melting

Fig. 5a-h shows the optical and BSE-SEM micrographs of the cross-sections of the IN718–ceramic (NbC, TiC, TiB_2) composite system after combined processing by SPS by laser surface melting. The rapid melting and solidification induced by high-energy laser irradiation substantially altered the original as-sintered microstructures.

The panoramic overview of the laser-melted layer of the composite (Fig. 5a) confirms the formation of a well-densified, continuous melt pool, with a fine cellular-dendritic pattern visible in Fig. 5b. At higher magnifications, the microstructure of the unreinforced IN-0 alloy (Fig. 5c) is characterized by a pronounced dendritic structure typical of rapid solidification. Bright white BSE-contrast equiaxed inclusions with angular, idiomorphic morphology are occasionally observed within the interdendritic areas. Concurrently, a thin, discontinuous network of a eutectic phase, predominantly attributed to the Laves phase, with bright BSE contrast is present in the interdendritic zones. The cores of the dendritic cells exhibit a uniform gray contrast corresponding to the single-phase γ (FCC) Ni-based solid solution, while the interdendritic

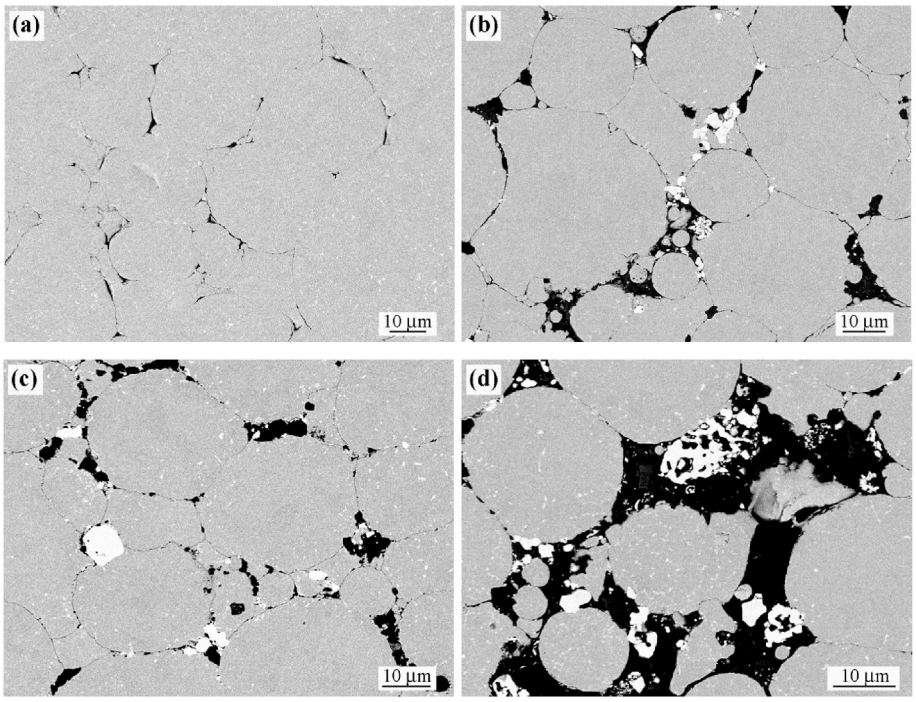

Fig. 3. BSE-SEM micrographs showing the microstructure of the IN718–ceramic composites processed via SPS at 1000 °C: (a) IN-0 (pure IN718, porosity: 0.49%), (b) IN-5, (c) IN-10, and (d) IN-20.

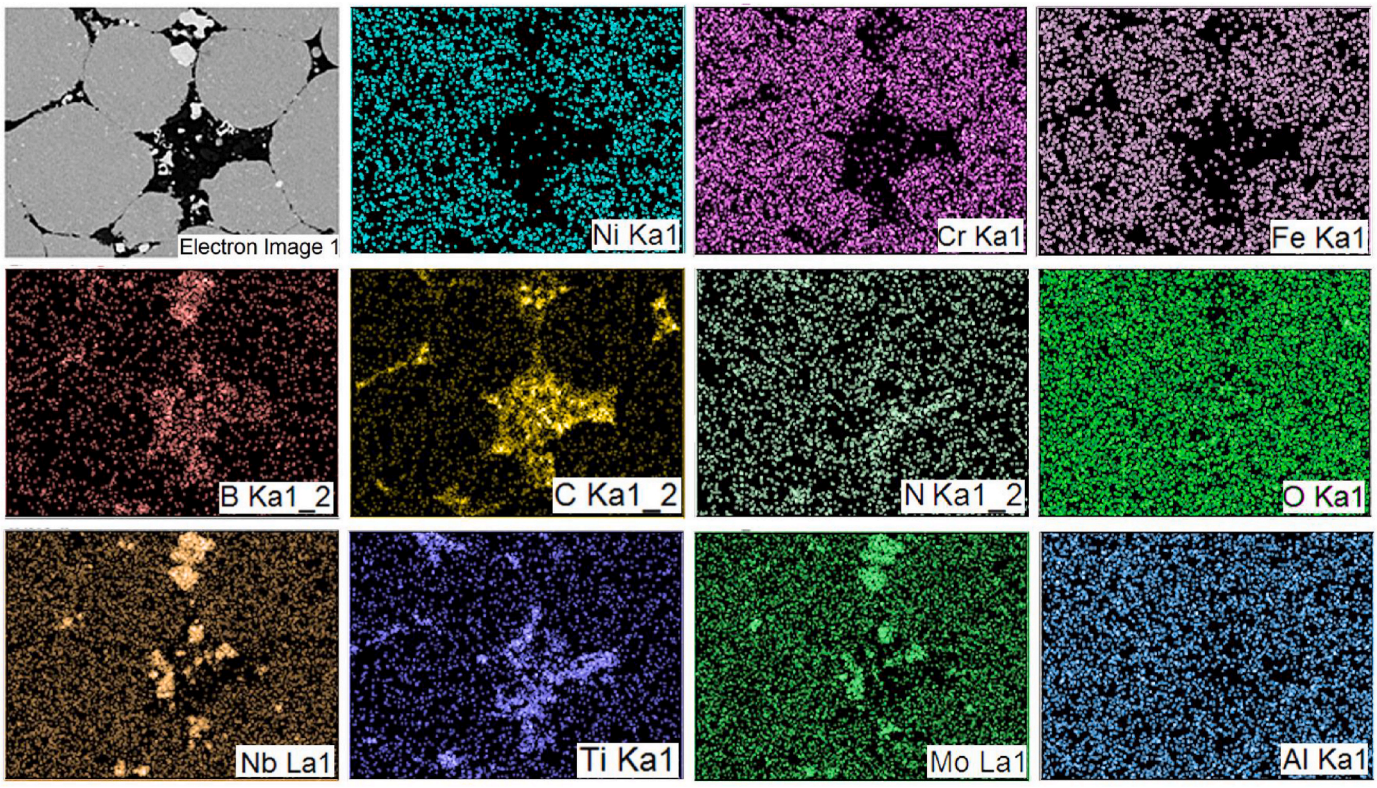

Fig. 4. SEM micrograph (electron image) and corresponding EDS elemental mapping (Ni, Cr, Fe, B, C, N, O, Nb, Ti, Mo, Al) of the as-sintered IN-10 composite, demonstrating interstitial phase separation and the localized distribution of titanium/niobium carbides and borides within the interparticle areas.

regions appear visually rougher due to the presence of numerous etching pits.

The addition of 5 vol% of the ceramic precursor significantly alters the crystallization behavior of the melt (Fig. 5d), resulting in: (a) a noticeable refinement of the dendritic structure, (b) a finer interdendritic eutectic network, and (c) an increased population of equiaxed particles that remain predominantly localized along the interdendritic boundaries. At a precursor content of 10 vol% (IN-10), the cellular-

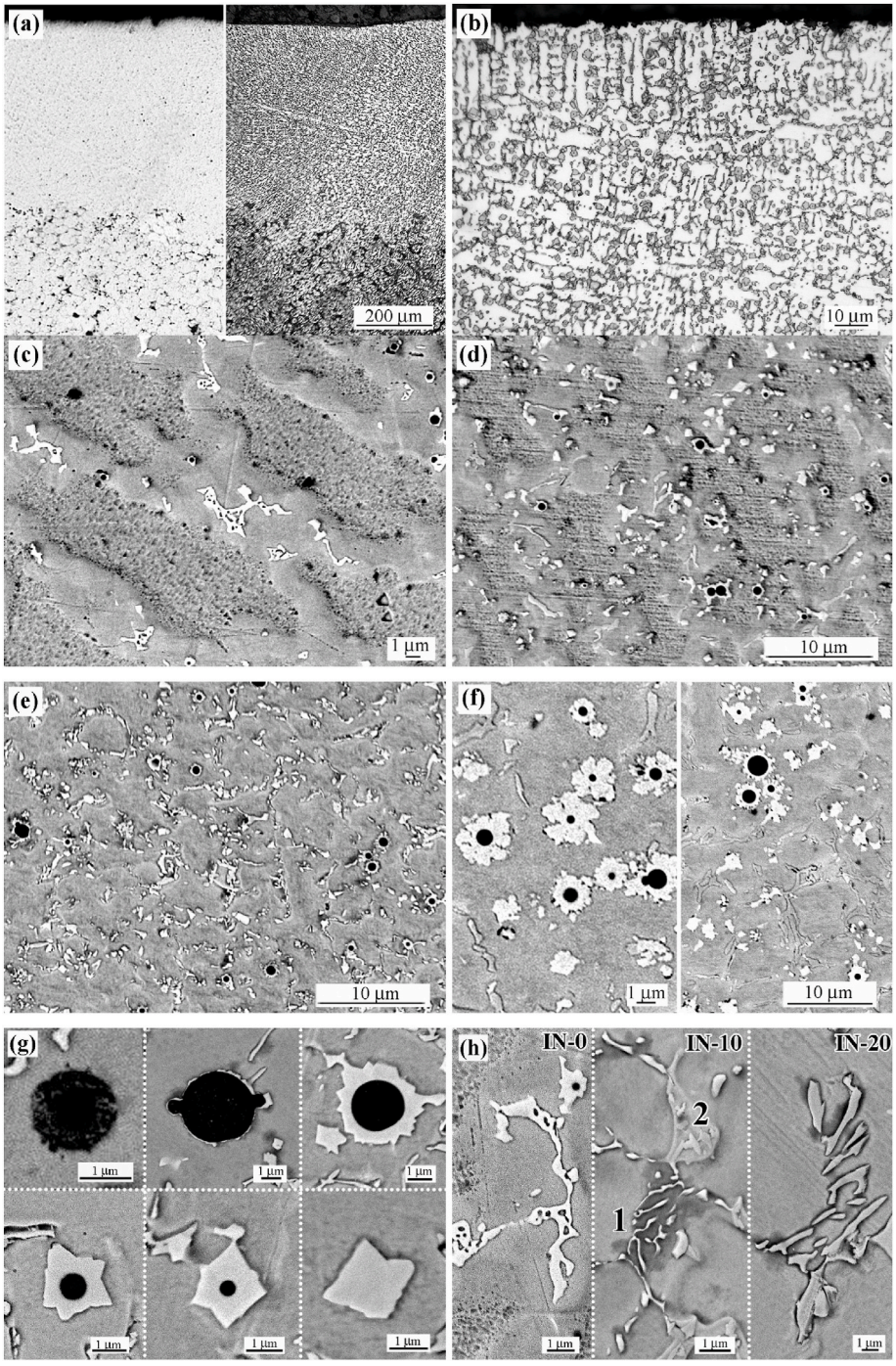

Fig. 5. Microstructural evolution after the combined SPS–LSM treatment: (a) cross-sectional overviews of the laser track in IN-20 in the unetched (left) and etched (right) states; (b) the dendritic pattern of the laser-melted zone in the IN-20 composite; (c–f) microstructures of IN-0, IN-5, IN-10, and IN-20, respectively; (g) morphological variations and the core-shell architecture of the equiaxed particles; and (h) alteration of the eutectic network topology in the IN-0, IN-10, and IN-20 specimens. (a, b: optical micrographs; c-h: SEM-BSE images).

dendritic matrix structure becomes less distinct, giving way to a highly heterogeneous dispersed structure (Fig. 5e), with a high density of fine inclusions distributed throughout the matrix. Under these conditions, the bright white equiaxed phases form multiple fine-crystalline clusters of a fragmented morphology, accompanied by an increased volume fraction of eutectic inclusions. At the maximum ceramic precursor content of 20 vol% (IN-20), laser processing produced a distinct composite structure characterized by pronounced phase agglomeration (Fig. 5f). Large conglomerates of coarse ceramic phases with faceted or fragmented morphologies are observed in the matrix, forming dense, island-like regions. Concurrently, the interdendritic eutectic network exhibits less pronounced bright BSE contrast and acquires a muted gray appearance, suggesting possible changes in its chemical or phase composition. Thus, laser remelting successfully transformed the original framework microstructure of the SPS composites into a dendritic, finely dispersed structure. As the ceramic precursor content rises from 0 to 20 vol%, the growth of IN718 dendrites becomes progressively restricted, consistent with growth-limited solidification and the formation of a refined cellular-dendritic morphology.

A distinctive feature of all modified composites is the presence of

equiaxed duplex particles comprising a dark BSE-contrast core surrounded by a bright-contrast shell (Fig. 5g). The dark core indicates enrichment in light elements, presumably oxygen, suggesting its oxide nature, whereas the bright shell is enriched in heavy elements, most likely Nb and Mo, consistent with a carbide origin. In all composites, the core-to-shell volume ratio varies widely, from particles consisting entirely of oxide or carbide to predominantly duplex core-shell structures (Fig. 5g). At the highest reinforcement level (IN-20), the carboboride shells lose their sharp faceting and develop a highly corrugated morphology with characteristic fringed edges (Fig. 5f).

The eutectic inclusion network also undergoes a pronounced morphological transformation (Fig. 5h). In the IN-0 reference alloy, this network exhibits a discontinuous character with a bright BSE contrast, enclosing isolated regions of the metallic matrix (Fig. 5h). In the metal–ceramic composites, the network changes in both morphology and BSE contrast. Two distinct morphological types of eutectics are observed in the IN-10 alloy: thin, tortuous plates resembling a "Chinese-script" type [51] with a high-Z contrast (designated as type 1 in Fig. 5h), and thicker, shorter plates with a low-Z contrast (type 2). In the highly reinforced IN-20 alloy, type 1 eutectic is completely eliminated, leaving only the low-Z-contrast type 2 eutectic.

Fig. 6 presents quantitative data on the size and number of inclusions as a function of ceramic filler content. As shown in Fig. 6a, the baseline IN-0 alloy contains 5.5% eutectic and 0.74% equiaxed inclusions by

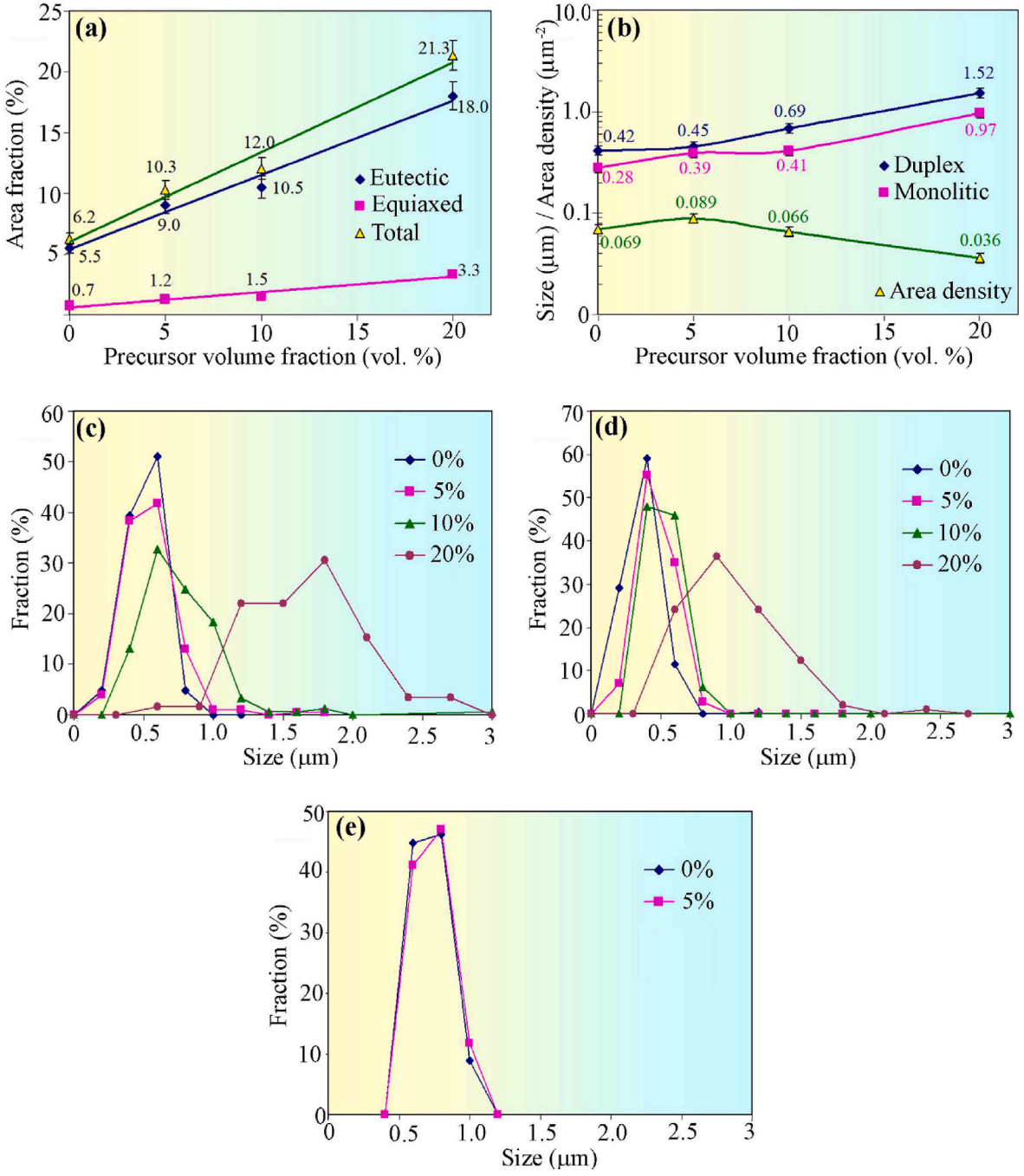

Fig. 6. Quantitative microstructural characterization of the composites as a function of precursor volume fraction: (a) phase area fractions; (b) average particle size and areal number density variations; and particle-size frequency distributions of different equiaxed inclusions types: (c) duplex core–shell, (d) monolithic, and (e) unshelled oxide inclusions (which are present only in IN-0 and IN-5).

area. With increasing ceramic content, both fractions rise, reaching 18.0% and 3.3%, respectively, in IN-20. The equiaxed inclusions also coarsen systematically: the average size of duplex inclusions increases from 0.42 to 1.52 μm, while that of monolithic inclusions increases from 0.28 to 0.97 μm (Fig. 6b). This coarsening is accompanied by a non-monotonic variation in particle number density, which peaks at 0.089 μm^{-2} in IN-5 before decreasing nearly threefold to 0.036 μm^{-2} in IN-20. The size-frequency distributions in Fig. 6c–d shows that both duplex and monolithic inclusions exhibit their most pronounced coarsening and rightward distribution shifts in IN-20. Pure, unshelled oxide inclusions (Fig. 6e) are detected only in the low-content IN-0 and IN-5 alloys and are not observed at higher precursor contents, where the oxide inclusions appear to be incorporated into core–shell architectures.

3.3. X-ray diffraction analysis

The phase constituents of the materials after the combined SPS–LSM treatment were analyzed by X-ray diffraction. According to the XRD patterns (Fig. 7), the IN-0 reference alloy (black line) is characterized by intense reflections corresponding to the face-centered cubic (FCC) γ-matrix solid solution. In addition, low-intensity peaks associated with primary niobium carbides (MC) and secondary phases, including the Laves phases Cr_2Nb, Ni_2Si, $CrSi_2$ and Cr_2Ti, as well as trace amounts of Al_2O_3, likely originating from the atomized industrial superalloy powder, are detected on the reference diffractogram.

The introduction of the multicomponent ceramic additive (NbC, TiC, TiB_2) leads to changes in the phase composition and diffraction profiles. As the initial ceramic content rises to 10 vol% (IN-10) and 20 vol% (IN-20), the intensity of the primary γ-matrix reflections decreases slightly, potentially reflecting a lower matrix fraction within the analyzed laser-modified layer and the formation of secondary phases. From the IN-5 to the IN-20, the reflection intensities associated with NbC and TiC increase monotonically, particularly in the 2θ range of 35–42°. The presence of TiB_2 is supported by characteristic minor reflections, whose number and intensity increase with filler content and reach their highest levels in the IN-20 composite. Concurrently, diffraction peaks that may correspond to Cr_7C_3, boride phases (Mo_2B_5 and Nb_3B_4), TiO_2, Laves-type compounds, and silicides such as ($CrSi_2$, Ni_2Si) are observed in the composite tracks. The detection of carbide and boride reflections suggests redistribution of carbon and boron and their interaction with alloying elements during the non-equilibrium thermal cycle. These results are consistent with dissolution of the ceramic constituents during laser processing, followed by enrichment of the melt pool in Ti, Nb, B, and C and the possible *in-situ* precipitation of new intermetallic, complex carbide, and boride phases during rapid solidification.

A key feature of the diffractograms is the limited number of distinct

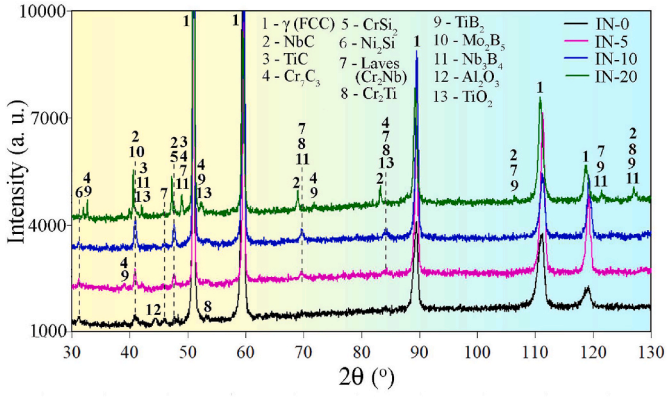

Fig. 7. XRD patterns of the reference IN-0 alloy and the modified IN-5, IN-10, and IN-20 composites after the combined SPS–LSM treatment. (1 – γ(FCC), 2 – NbC, 3 – TiC, 4 – Cr_7C_3, 5 – $CrSi_2$, 6 – Ni_2Si, 7 – Laves phase (Cr_2Nb), 8 – Cr_2Ti, 9 – TiB_2, 10 – Mo_2B_5, 11 – Nb_3B_4, 12 – Al_2O_3, 13 – TiO_2).

reflections that can be unambiguously assigned to a single phase, such as the γ-matrix, NbC, or TiC. The close structural similarity and comparable lattice parameters of the coexisting matrix and reaction products result in substantial overlap of diffraction peaks across the entire 2θ range. Consequently, the presence of chromium carbide and specific intermetallic compounds cannot be unequivocally established from the XRD data alone and should therefore be regarded as tentative. Nevertheless, the XRD analysis confirms the composite nature of the resulting structure, consisting of a metallic γ-matrix and ceramic reinforcement.

3.4. EDS and EPMA characterization of phase elemental distribution

The elemental partitioning within the laser-modified layers is summarized in Tables 2 and 3 and Figs. 8–10, based on the EDS point analyses and elemental mapping. In the reference IN-0 alloy, the matrix dendrite cores consist predominantly of a Ni-based solid solution (55.2 wt% Ni, 19.0 wt% Cr, 19.2 wt% Fe) and are strongly depleted in Nb (2.4 wt%) (Table 2). In contrast, Nb is strongly segregates into the interdendritic liquid, reaching 5.6 wt% in the interdendritic areas. This localized supersaturation promotes the precipitation of secondary phases. The bright interdendritic eutectic blocks exhibit pronounced Nb enrichment (21.2 ± 7.5 wt%), characteristic of the Laves phase. The discrete equiaxed particles contain higher Nb level (27.8 wt%) and less Ni (34.3 wt%). Given the extremely low carbon content of the base IN718 alloy, these equiaxed particles are more likely Laves-phase precipitates than primary NbC. The presence of submicron dark cores, together with the detected oxygen content (0.6 wt%) suggests heterogeneous nucleation of refractory oxide inclusions, which may subsequently serve as substrates for Laves-phase growth.

The distinctive features of the laser-processed IN718–ceramic composites are the equiaxed monolithic and duplex core-shell particles. Fig. 8a shows a high-resolution SEM-BSE micrograph and corresponding EDS elemental maps (O, Ti, Al, N, Nb, B, C, Mo, Cr, Fe, and Ni) of two duplex inclusions in the IN-20 composite. These particles comprise a rounded, low-Z contrast (dark) core encapsulated by a faceted, high-Z contrast (bright) shell. The EDS maps reveal clear elemental partitioning between these two zones, providing insight into their *in-situ* formation mechanism. The inner spheroidal core exhibits intense Ti, O, and Al enrichment (40.1 wt%, 38.0 wt%, and 16.9 wt%, respectively), accounting for its dark contrast in BSE images. A nitrogen signal is detected within this inner domain, although its mapping intensity is low. The core is also depleted in the main matrix elements (Ni, Fe, and Cr), consistent with its identification as a Ti–Al-rich oxide that acted as an endogenous substrate. The outer shell is strongly enriched in Nb, Mo, C, and B, suggesting that a complex carboboride epitaxially formed around the pre-existing oxide core. The sharp drop in Ni, Fe, and Cr signals at the matrix–particle interface further indicates their near-zero solubility in the synthesized inclusion.

The specific phase elemental compositions were clarified using point EDS analysis, (Table 3; Fig. 9). The point analysis confirms a highly

Table 2
Phase elemental compositions (wt.%) in the reference IN-0 alloy after the combined SPS–LSM treatment.

Elements	Equiaxed particles	Eutectic	Matrix	
			dendrite body	interdendritic area
Si	0.2 ± 0.05	0.4 ± 0.05	–	0.2 ± 0.05
O	0.6 ± 0.2	–	–	–
Ti	0.3 ± 0.1	0.6 ± 0.1	0.6 ± 0.1	–
Cr	14.8 ± 1.1	15.8 ± 1.4	19.0 ± 2.3	16.2 ± 1.3
Ni	34.3 ± 2.8	43.9 ± 6.0	55.2 ± 3.9	57.7 ± 3.2
Nb	27.8 ± 3.4	21.2 ± 7.5	2.4 ± 0.4	5.6 ± 0.4
Mo	2.7 ± 0.3	4.8 ± 1.0	3.0 ± 0.5	3.3 ± 0.4
Al	0.2 ± 0.05	0.2 ± 0.05	–	–
Fe	11.8 ± 1.5	13.1 ± 1.8	19.2 ± 2.3	17.0 ± 1.1

Table 3
Phase elemental compositions (wt.%) in the highly reinforced IN-20 composite after the combined SPS–LSM treatment.

Elements	Equiaxed particles		Eutectic particles	Matrix
	Monolithic and shell in duplex particles	Oxide core		
B	17.9 ± 6.8	–	23.20 ± 1.9	–
C	12.9 ± 2.9	–	–	–
O	–	38.0 ± 1.5	–	–
Ti	4.3 ± 1.3	40.1 ± 1.6	0.8 ± 0.3	0.3 ± 0.1
Cr	2.9 ± 0.7	3.8 ± 0.9	19.3 ± 0.4	17.7 ± 1.2
Ni	–	1.2 ± 0.5	10.4 ± 2.8	58.7 ± 2.3
Nb	58.8 ± 3.5	–	29.4 ± 2.1	2.6 ± 0.6
Mo	3.2 ± 0.7	–	12.5 ± 0.2	2.2 ± 0.9
Al	–	16.9 ± 0.3	–	0.2 ± 0.1
Fe	–	–	4.4 ± 0.5	18.3 ± 1.5

heterogeneous phase state. The equiaxed monolithic particles and the shells of duplex particles are composed predominantly of Nb (59.0 wt %), B (18.7 wt%), and C (12.9 wt%), consistent with the formation of Nb-rich complex carboborides containing minor amounts of Ti, Cr, and Mo (Fig. 9a). In contrast, the dark core region consists of a complex oxide phase containing 40.1 wt% Ti, 38.0 wt% O, and 16.9 wt% Al. Although the elemental maps show a weak N signal in this region, nitrogen was not detected in the point EDS quantification. The oxide core may have formed through high-temperature oxidation during laser processing in ambient air. The high thermodynamic affinity of Ti and Al for oxygen could promote the formation of a complex Al–Ti oxide during the early stages of solidification.

Fig. 8b presents an interdendritic eutectic network adjacent to an angular high-BSE-contrast monolithic phase. The elongated, script-like inclusions are enriched in B, Nb, Cr, and Mo relative to the matrix, as confirmed by the point EDS data in Table 3 and the spectra in Fig. 9b and c. The spatial co-localization of these elements is consistent with the formation of *in-situ* (Nb,Cr,Mo,Ti)-rich borides. The uniform distribution of Al, Si, and O indicates that primary oxide inclusions were not directly involved in eutectic formation. The larger angular particle on the right features a high, localized concentration of Nb, Mo, C, and B, consistent with its identification as a complex Nb-based carboboride rather than a metallic Laves phase.

The higher volume fraction of the eutectic constituent in the ceramic-containing composites suggests that the precursor particles partially dissolved during laser processing, followed by the reactive precipitation of solute elements from the melt. To evaluate the extent of precursor dissolution, the distribution of the main ceramic constituents (Nb, Ti, C, and B) was examined by EPMA. As shown in Fig. 10, titanium is detected in all equiaxed inclusions but is concentrated mainly in the Ti–Al-rich oxide cores of duplex particles. The carbon distribution largely overlaps with that of titanium. Niobium is detected in both equiaxed and eutectic phases, with higher concentrations in the equiaxed inclusions. Boron shows a similar to niobium distribution across the reinforcing phases. Within the eutectic network, Nb and B are co-localized with Mo, which is confined exclusively to the eutectic network. The overall distribution patterns remain similar at different precursor contents (Fig. 10a and b). Notably, EPMA revealed no monoelemental inclusions containing only Nb or Ti, or inclusions containing only Ti and B, which could indicate the persistence of unmolten NbC, TiC, or TiB_2 precursor particles. Instead, all equiaxed inclusions simultaneously contain Nb, Ti, C, and B, whereas the eutectic network contains Nb and B. This elemental co-localization is consistent with extensive dissolution of the ceramic precursors in the melt pool and the subsequent *in-situ* formation of multicomponent equiaxed carboborides and eutectic borides.

Some of the solute Nb and B partitioned into the interdenritic zones, where these elements reacted with Mo and Cr (Fig. 9b), forming a boride eutectic containing 29.4 wt% Nb (Table 3). This phase may be more stable under processing conditions than the Laves phase typically found in IN718 alloy. Meanwhile, the matrix grains retain a typical IN718 chemistry, consisting primarily of Ni (58.7 wt%), Fe (18.3 wt%), and Cr (17.7 wt%), with a lower Nb content (2.6 wt%) compared to the eutectic zones (Fig. 10c). These results indicate that a substantial fraction of the added Nb was effectively incorporated into the *in-situ* synthesis carboboride and eutectic phases during the laser processing stage.

3.5. Nanoindentation testing results

The micromechanical response of the fabricated materials as a function of the ceramic filler volume fraction is illustrated in Fig. 11. As shown in Fig. 11a, both the average indentation modulus and indentation hardness increase nonlinearly with ceramic content. For the unreinforced IN-0 reference alloy, the baseline modulus and hardness are 200.4 ± 2.4 GPa and 3.22 ± 0.09 GPa, respectively. The addition of 5 vol % (IN-5) and 10 vol% (IN-10) ceramic filler produces modest changes in both properties. A more pronounced effect is observed in IN-20, at 20 vol % of ceramics filler, where the indentation modulus reaches 228.7 ± 2.9 GPa and the indentation hardness increases to 4.38 ± 0.05 GPa. These values correspond to increases of approximately 14% in modulus and 36% in hardness relative to the unreinforced reference alloy.

The load–displacement curves recorded at a maximum load of 500 mN further illustrate the differences in mechanical response (Fig. 11b). The loading slopes become progressively steeper from the IN-0 to the IN-20 configuration, reflecting higher contact stiffness. At the same maximum load, the penetration depth decreases from approximately 2600 nm for IN-0 to 2250 nm for IN-20. The residual depth after unloading also decreases, indicating greater resistance to permanent deformation in the composite with the highest content of the *in-situ* synthesized ceramics.

Fig. 11c displays the evolution of the elastic recovery index (*ERI*), plasticity index (*PI*), and the h_p/h_{max} ratio, which are energy-based parameters that effectively characterize the elastoplastic mechanical behavior of the alloy. The *ERI* values increases slightly from 0.191 (IN-0) to a maximum of 0.230 at 10 vol% of ceramics filler (IN-10), indicating a superior capability of the material for elastic recovery during unloading at this concentration. It then drops slightly to 0.211 for IN-20. In contrast, the *PI* decreases from 0.809 to a minimum of 0.770 at 10 vol% ceramics filler before rising slightly to 0.789 for IN-20. These opposite trends confirms an enhanced capacity for elastic energy storage in the composite states. The h_p/h_{max} ratio remains relatively stable, ranging from 0.881 to 0.902 across all compositions, demonstrating that plastic deformation remains the dominant during localized loading, even in the highly reinforced composite.

3.6. Tribological behaviours

The friction coefficient (CoF) over 2000 sliding cycles under dry conditions against a WC counterbody is illustrated in Fig. 12a. During the initial running-in stage, which lasts approximately 250 cycles, all composites exhibit sharp CoF fluctuations as surface asperities are worn down and the contact geometry stabilizes. After this initial stage, the friction tracks reach steady-state sliding conditions.

The IN-0 reference alloy displays the most erratic friction profile with the highest initial run-in peaks, before reaching an average CoF of 0.95 ± 0.11 during the final 1000 cycles. The addition of 5 vol% ceramic mixture (IN-5) results in only a minor change, with a steady-state average CoF of 0.92 ± 0.07. A more pronounced CoF reduction is observed for the IN-10 composite, which exhibits a more stable friction profile and a final average CoF of 0.86 ± 0.05. In contrast, the heavily reinforced IN-20 composite demonstrates a sharp drop in CoF after 600 cycles, reaching the lowest average CoF value of 0.77 ± 0.11. However, the CoF curve for IN-20 shows more high-frequency fluctuations toward the end of the test.

The three-dimensional (3D) surface topographies of the resulting

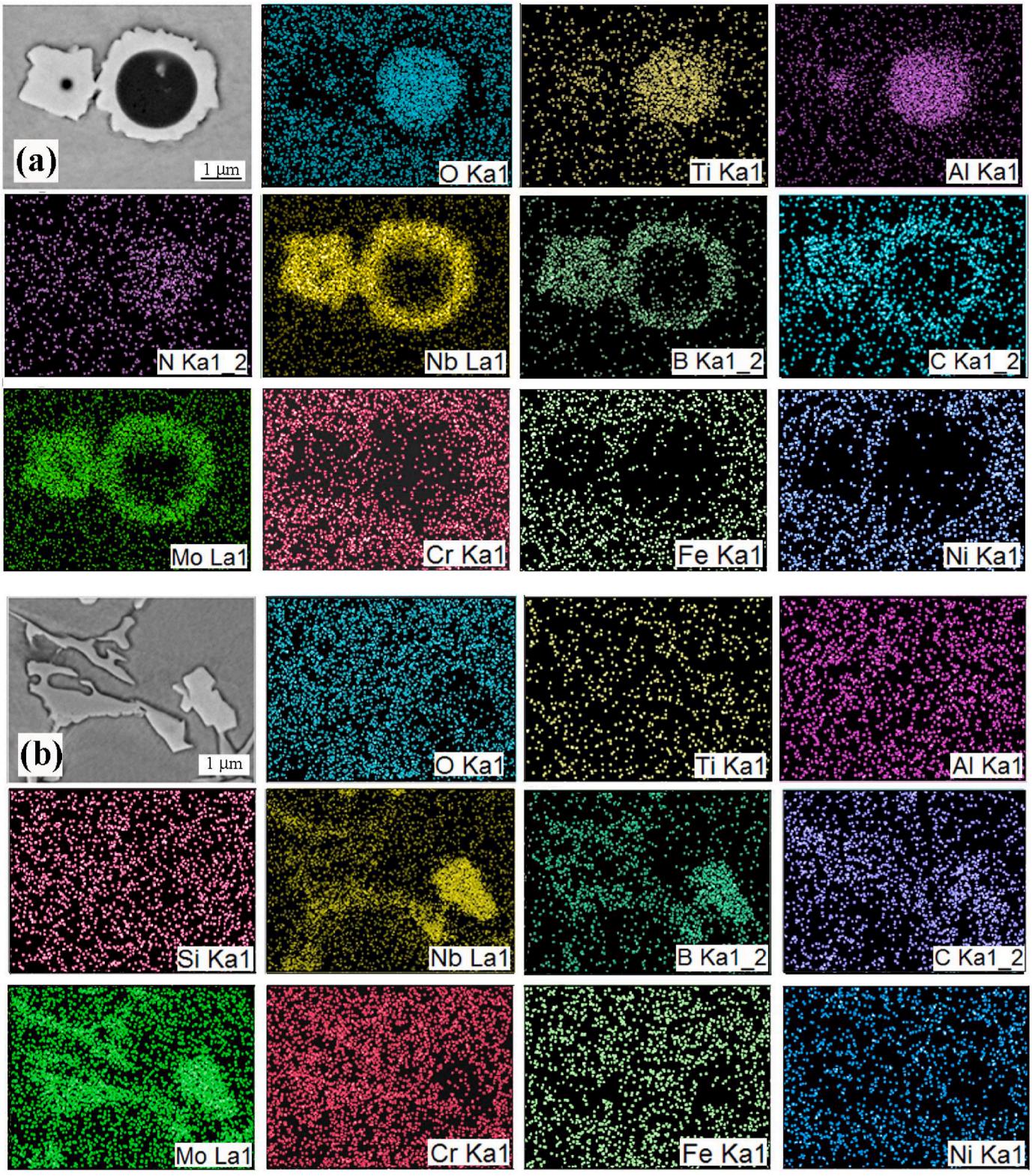

Fig. 8. SEM-BSE micrographs and corresponding EDS elemental maps of the laser-processed IN-20 composite showing: (a) equiaxed core–shell inclusions and (b) an interdendritic region containing a eutectic network adjacent to an angular monolithic compound.

wear tracks are presented in Fig. 13, while the corresponding cross-sectional and longitudinal profiles and wear rate are shown in Fig. 12b-d. The 3D topography of the unreinforced IN-0 alloy (Fig. 13a and b) reveals a severely worn track with a rough, torn surface, deep longitudinal valleys, and irregular edges, signaling substantial material removal. The addition of 5 vol% ceramic filler (Fig. 13c) produces little change in the track morphology, which remains wide and rough, with slight lateral material pile-up along the edges. In the IN-10 composite (Fig. 13d), the wear track becomes narrower, straighter, and more uniform, with a smoother floor, indicating improved resistance to micro-ploughing. In contrast, the track in the highly reinforced IN-20 composite (Fig. 13e) exhibits pronounced geometric heterogeneity, with a

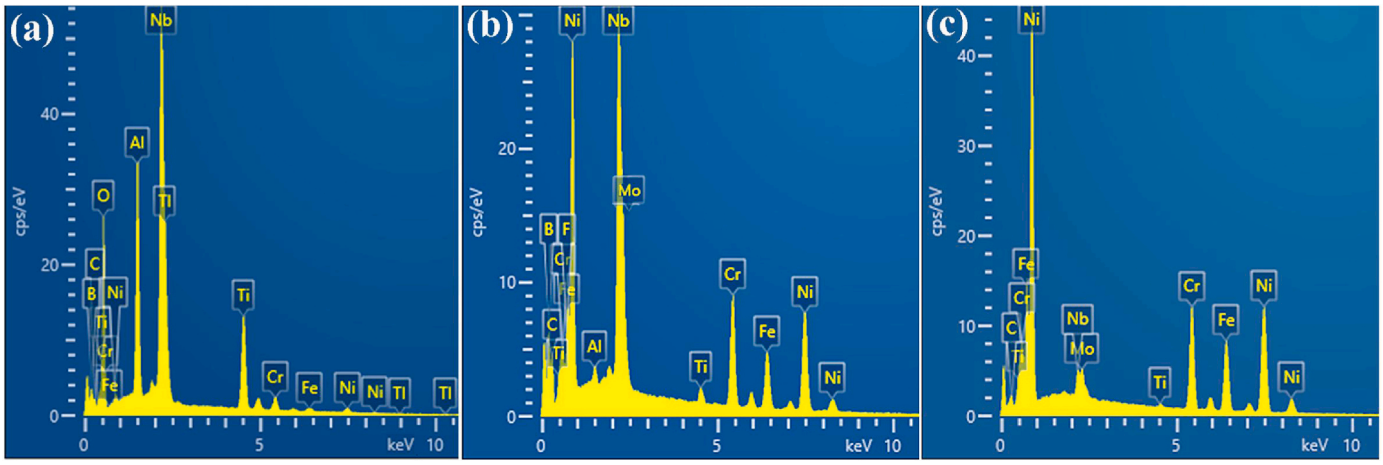

Fig. 9. Point EDS spectra of individual structural constituents in the IN-20 composite: (a) equiaxed duplex particle showing the combined signals of the Ti–Al-rich oxide core and Nb-rich shell, (b) interdendritic complex eutectic boride phase, and (c) core of the nickel-based γ-matrix core.

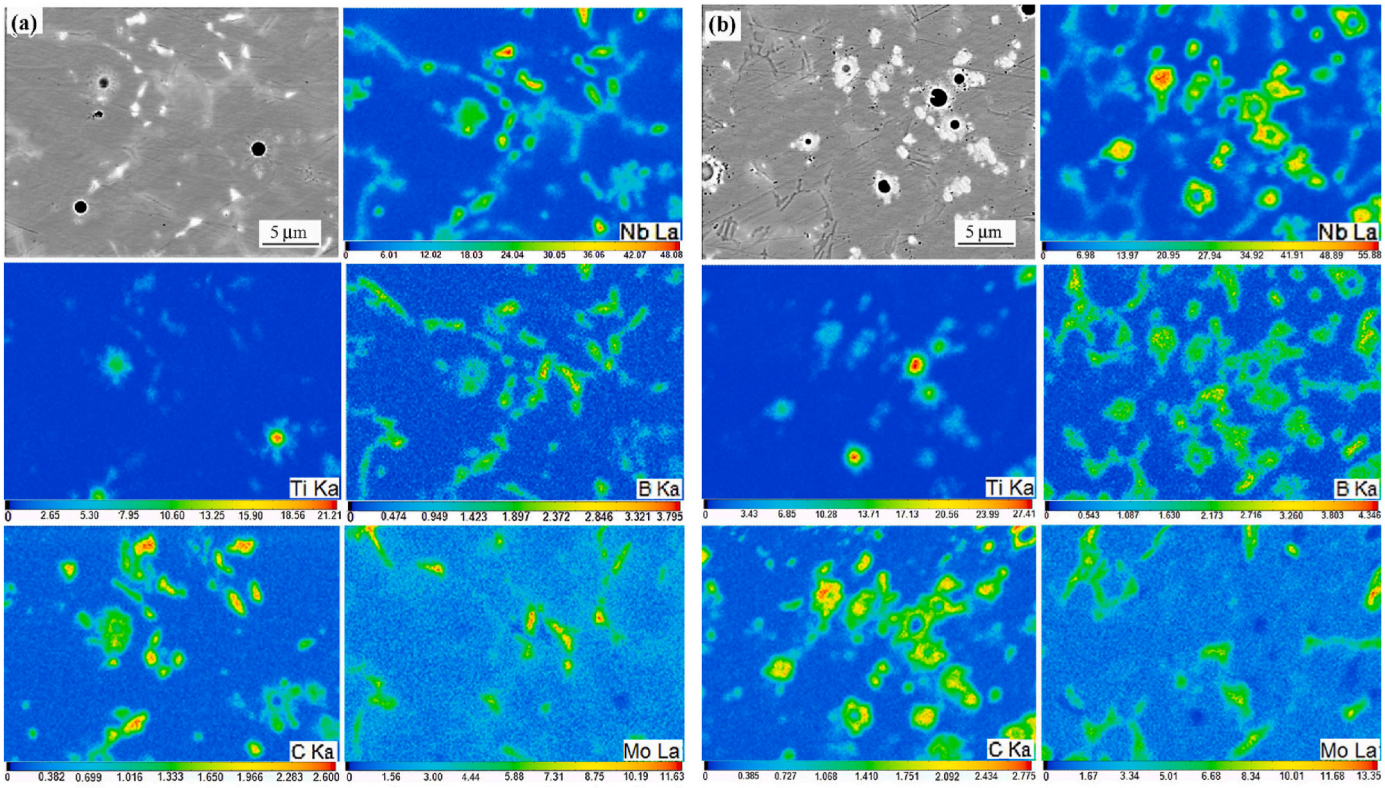

Fig. 10. EPMA elemental maps of C, B, Nb, Ti and Mo within the (a) IN-5 and (b) IN-20 composite structures.

wave-like profile along the sliding direction and alternating wear craters and material protrusions. Across all compositions, the lateral pile-up along the track boundaries remains small compared with the depth of the wear valleys. This suggests that material removal and delamination, rather than plastic displacement alone, contributed substantially to wear.

These trends are consistent with the cross-sectional profiles (Fig. 12b), longitudinal depth profiles (Fig. 12c), and wear rates (Fig. 12d). The cross-sectional profiles show that IN-0 and IN-5 develop deep, wide, U-shaped scars with little lateral pile-up, suggesting that wear debris is removed from the contact zone. Introducing ceramic filler reduces the track width and depth, the IN-10 track reaching a depth of approximately 14 μm. In contrast, the IN-20 track (Fig. 12c) features pronounced fluctuations in depth along the sliding direction. Two profiles are shown: the solid line represents the deepest wear crater, whereas the dashed line corresponds to the protruding region, where the track depth is only approximately 2-5 μm.

Fig. 12d shows a substantial, monotonic improvement in wear resistance with increasing ceramic filler content. The unreinforced IN-0 alloy suffers the most severe degradation, exhibiting the highest wear rate of 2.31×10^{-4} mm^3/(N·m). A slight reduction in wear rate is recorded for the IN-5 composite (2.19×10^{-4} mm^3/(N·m)), followed by a more pronounced decrease to 1.43×10^{-4} mm^3/(N·m) for the IN-10 composite layer. The lowest wear rate is observed for the IN-20 composite track, at 0.97×10^{-4} mm^3/(N·m), representing a reduction of approximately 58% relative to the unreinforced IN718 alloy.

SEM analysis of the unreinforced IN-0 wear surface reveals several wear mechanisms (Fig. 14a–c), including plastic deformation, adhesion,

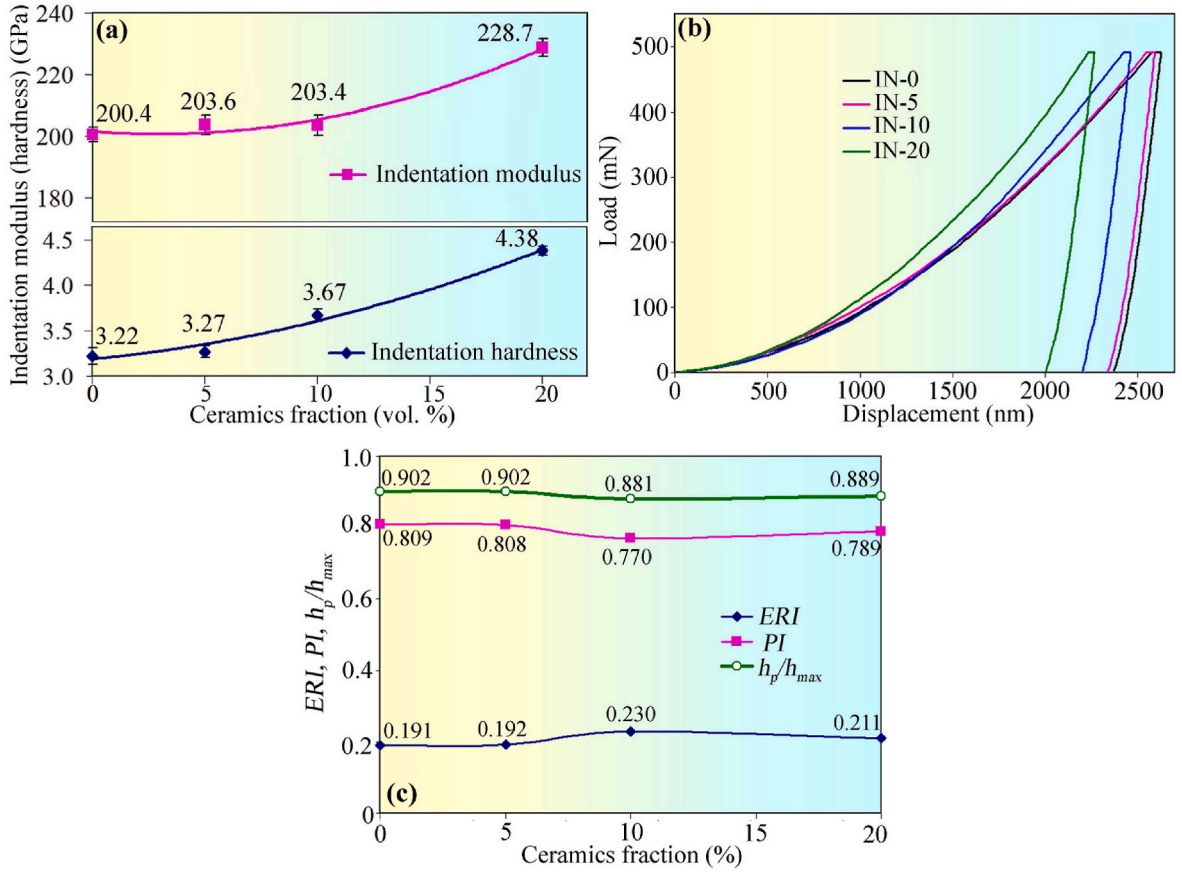

Fig. 11. Results of nanoindentation testing: (a) effect of the ceramic filler volume fraction on the average indentation modulus and indentation hardness of the combined SPS–LSM treated layers; (b) representative load–displacement curves for the IN-0, IN-5, IN-10, and IN-20 configurations; (c) effect of the ceramic filler volume fraction on the *ERI*, *PI*, and h_p/h_{max} values.

tribochemical oxidation, and tribolayer delamination. The track overview (Fig. 14a) shows deep grooves with lateral ridges formed by material displacement, as well as localized areas of adhesive interaction and metal pull-out. Approximately one-third of the track surface is covered by thinned tribolayer films (Fig. 14b) with multiple cracks, indicative of a pre-fractured state (Fig. 14c). In areas where the films have delaminated, the surface is covered with agglomerates of fine debris and fragmented oxide films (Fig. 14d).

Incorporating ceramic phases into the IN718 matrix changed the wear behavior, reducing both the friction coefficient and material loss. SEM micrographs of the IN-20 track (Fig. 14e and f) demonstrate a more uniform surface morphology than that of the unreinforced alloy. The track surface is uniformly covered with thin, densely compacted flakes forming a protective a mechanically stable protective tribo-layer (Fig. 14d), while relatively large tribo-films similar to those observed on the IN-0 sample (Fig. 14a) are rare. The hard *in-situ* ceramic particles may limit deep plastic deformation and promote the retention and compaction of fine debris and oxides within the contact zone. The overview (Fig. 14e) shows fewer signs of delamination; the deep cracks in the oxide films and their large-scale spallation, characteristic of the unreinforced matrix, are largely suppressed. The sliding track is marked by shallow, parallel micro-ploughing grooves. The improved wear resistance is therefore associated with the formation of a dense, compacted tribolayer that limits adhesive wear and subsurface delamination.

To evaluate tribo-oxidation behaviour, an EDS line scan and oxygen mapping were performed across the wear tracks (Fig. 15). On the unreinforced IN-0 surface (Fig. 15a), the oxygen signal varies across the track but remains relatively high (18.8-22.3 wt%, Table 4), with no clear correlation between oxygen content and the visible boundaries of oxide-covered regions. This suggests widespread oxidation of the matrix alongside extensive plastic deformation, which may contribute to embrittlement and delamination. In contrast, oxidation in the IN-20 composite (Fig. 15b) is more localized. The oxygen content reaches 19.1 wt% within the thick oxide patch and drops to 4.3 wt% in the adjacent delamination zone (Table 4). This distribution is consistent with localized oxidation in the composite track, although the EDS data alone cannot establish whether the carboboride phase restricts strain or oxygen diffusion. Oxidation appears to be concentrated mainly within thin surface flakes, which may help maintain stable frictional contact. Furthermore, the high local concentrations of Ni (43.9 wt%) and Cr (21.3 wt%) in the IN-20 delamination zones are atributted to exposure of the underlying matrix following tribofilm removal, allowing its elemental composition to be detected by EDS.

The deformation behavior of the material directly beneath the wear-track surface, in the longitudinal direction of the track, is shown in Fig. 16. In the unreinforced IN-0 specimen, the wear-track surface exhibits an irregular morphology consisting of alternating protrusions and depressions formed by localized plastic flow at adhesion sites associated with individual asperities up to 10 μm in length (Fig. 16b). No microcracks or voids were observed either immediately beneath the surface or deeper below the wear track. In the IN-20 specimen (a region characterized by a shallow surface relief is shown), the wear-track surface is comparatively smooth and exhibits clear evidence of plastic flow within the near-surface layers (Fig. 16c). Intense plastic deformation extends to a depth of approximately 10 μm and is manifested by slip bands aligned with the principal direction of the applied shear stresses, forming a fibrous microstructure oriiented along the sliding direction (Fig. 16d). The density of the fibers reaches a maximum immediately beneath the surface, and no discontinuities between adjacent fibers were observed.

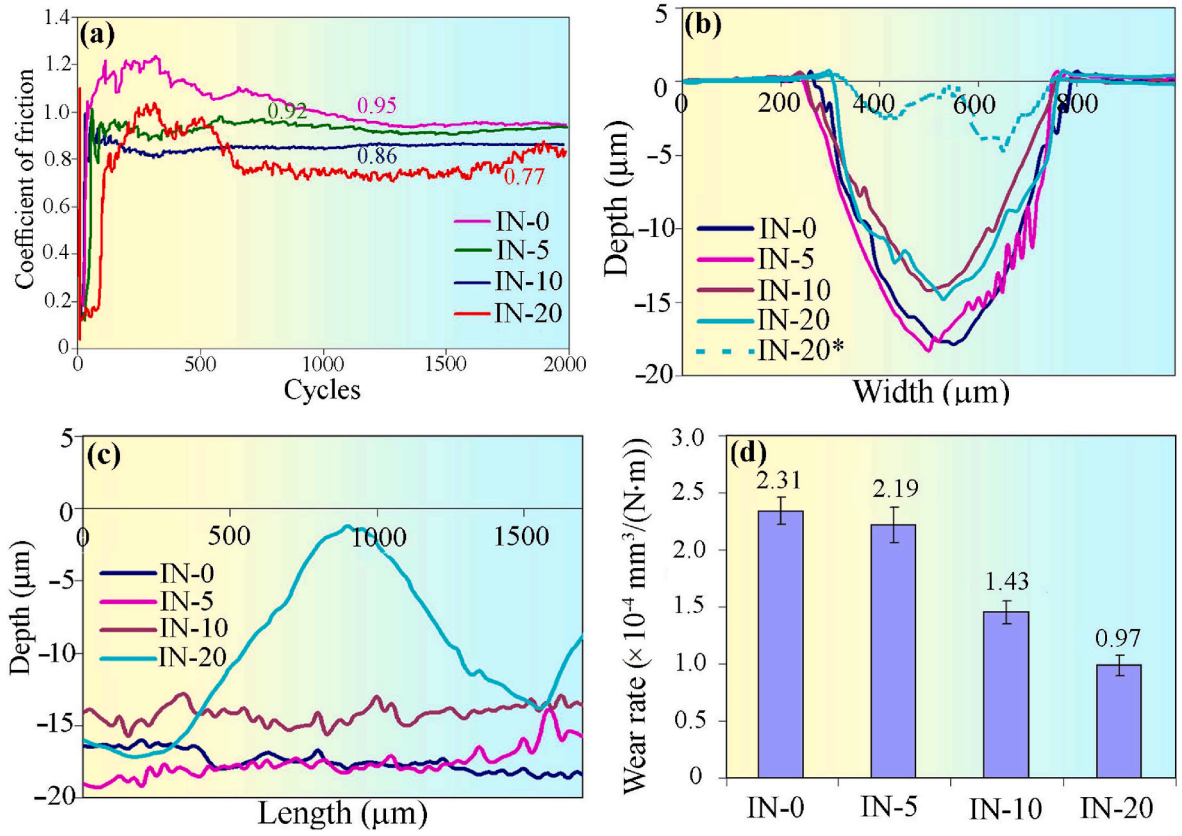

Fig. 12. Quantitative analysis for the IN718–ceramic composite wear tracks: (a) friction coefficient as a function of sliding cycles over 2000 cycles; (b) transverse cross-sectional profiles across individual wear tracks; (c) longitudinal depth profiles along the sliding direction; and (d) wear rates of the tested specimens. (The asterisk in (b) denotes the IN-20 cross-sectional profile measured across the protruding wear-resistant tribo-pad).

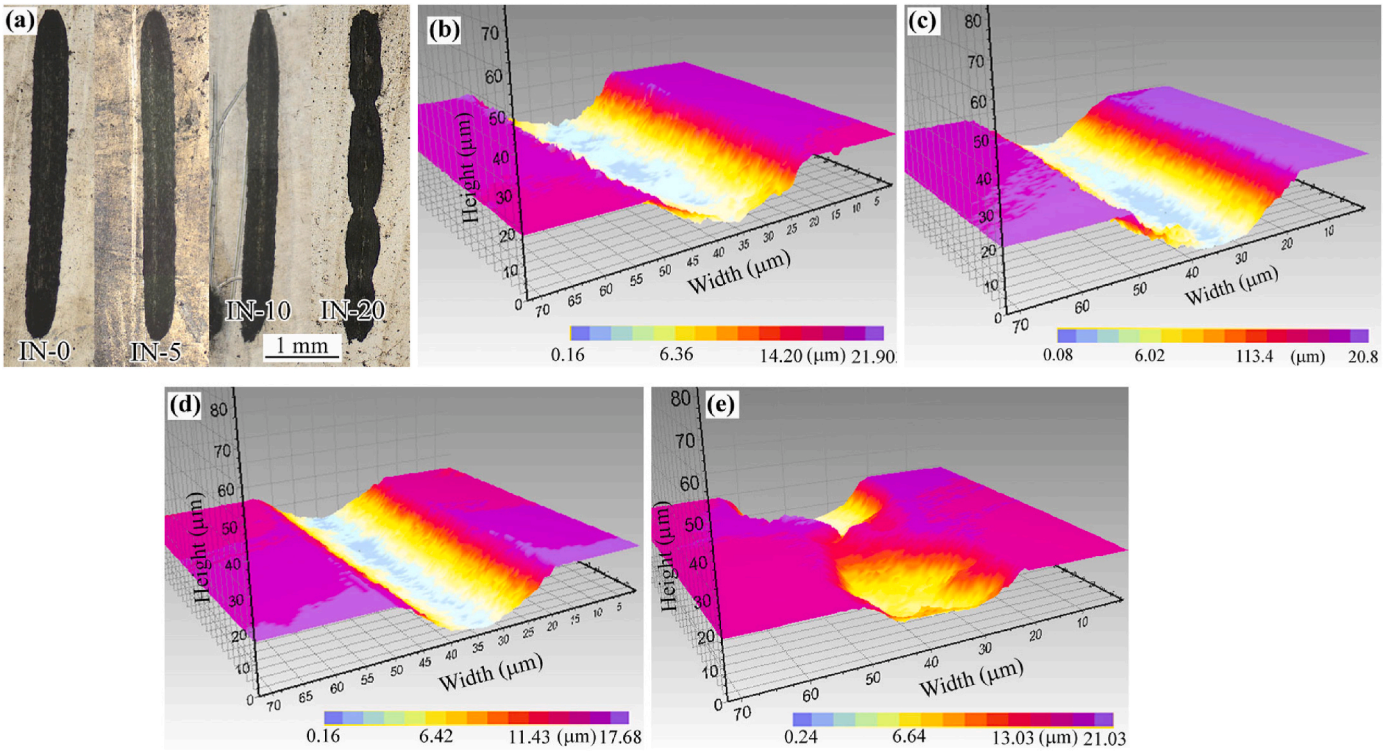

Fig. 13. Wear track morphology: (a) optical micrographs and (b–e) corresponding 3D surface profiles of the tracks for IN-0, IN-5, IN-10, and IN-20 samples, respectively.

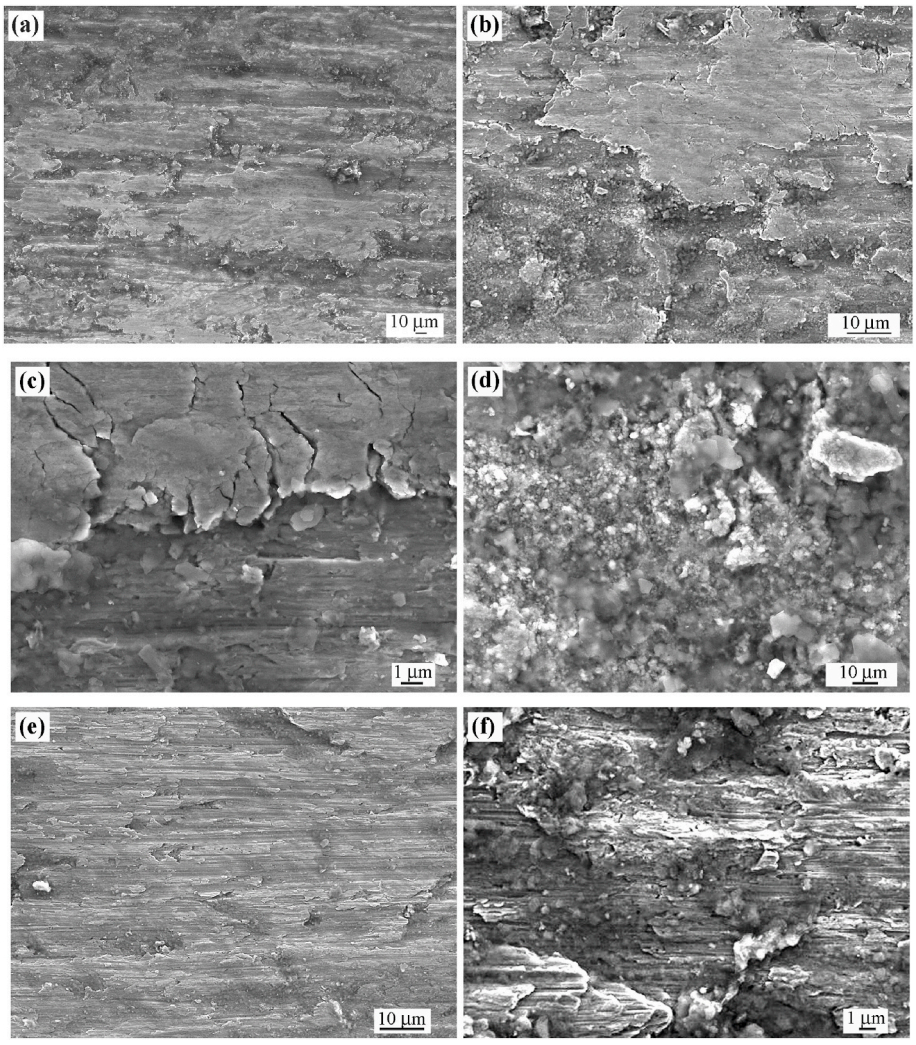

Fig. 14. SEM micrographs detailing the wear track morphology and characteristic degradation mechanisms: (a-d) intense plastic plactic deformation and tribo-oxidation in the IN-0 alloy; (e, f) mild abrasive micro-ploughing and stable, protective compacted tribo-layer formation in the IN-20 composite.

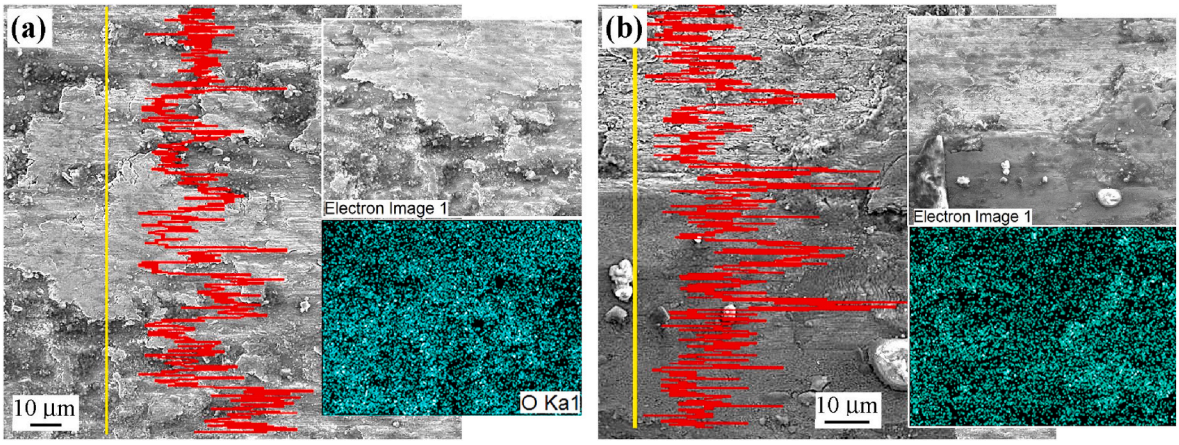

Fig. 15. EDS oxygen distribution analysis across the worn track surfaces: (a) linear intensity profile and corresponding elemental mapping inset for the unreinforced IN-0 alloy; (b) linear intensity profile and corresponding elemental mapping inset for the highly reinforced IN-20 composite.

At a depth of approximately 10 μm, near the location of maximum fiber curvature, localized microvoids were detected at the carboboride particle/matrix interfaces (indicated by arrows in Fig. 16d).

Table 4
Point EDS analysis results (wt.%) of the worn surfaces for the IN-0 alloy and IN-20 composite.

Elements	IN-0		IN-20	
	Coarse oxide scale	Delamination area	Coarse oxide scale	Delamination area
O	18.8 ± 5.5	22.3 ± 13.5	19.1 ± 3.3	4.3 ± 0.2
Al	2.0 ± 0.4	4.5 ± 2.3	0.9 ± 0.3	0.4 ± 0.1
Si	1.7 ± 0.4	4.2 ± 1.1	0.5 ± 0.1	0.3 ± 0.1
Ti	0.3 ± 0.1	0.8 ± 0.3	0.6 ± 0.3	0.8 ± 0.2
Cr	18.1 ± 1.4	18.8 ± 3.1	14.9 ± 1.1	21.3 ± 2.3
Fe	15.1 ± 1.3	14.6 ± 5.6	11.4 ± 2.1	18,0 ± 1.1
Ni	35.4 ± 10.1	21.4 ± 14.5	29.7 ± 9.5	43.9 ± 6.2
Nb	4.8 ± 1.2	9.5 ± 2.6	18.0 ± 9.9	7.2 ± 1.3
Mo	3.3 ± 0.8	4.1 ± 1.1	5.0 ± 1.8	3.9 ± 0.5

4. Discussion

4.1. Laser-induced thermodynamic alterations and multicomponent non-equilibrium solidification pathway

The transition from an SPS heterophase framework to an LSM state triggers non-equilibrium metallurgical reactions in the transient molten pool. Under the high-energy-density fiber laser, the system experiences intense localized heating and Marangoni convection [52]. This cycle promotes the dissociation and dissolution of the precursor mixture (NbC–TiC–TiB_2) into the molten nickel-based alloy. Since the melting points of these refractory compounds far exceed the melting point of nickel, their decomposition presumably proceeds via contact melting and reactive diffusion at the matrix-ceramic interfaces rather than through pure thermal fusion [53,54]. The EPMA mapping (Fig. 9) shows no isolated regions dominated by a single precursor element. Had the precursor remained as unmelted *ex-situ* particles after the LSM cycle, distinct signal-rich regions corresponding to their constituent elements might have been observed. Instead, the spatial distribution demonstrates the co-localization of all four introduced elements (Nb, Ti, C, and B) within the *in-situ* precipitates (Fig. 9a and b), consistent with solute redistribution during melting and Marangoni-driven transport**.** Under rapid cooling, the solutes underwent joint *in-situ* co-crystallization, producing duplex oxide-carboboride inclusions, while residual boron appears to partition into interdendritic areasm, to form where complex eutectic borides may form.

Thermodynamic simulations (Fig. 2) show that adding the (NbC–TiC–TiB_2) precursor alters the phase equilibrium and solidification path. The Nb concentration doubles to 10.45 wt% and the Ti content increases sevenfold in IN-20 (Table 1), while the predicted liquidus temperature rises from 1350 °C (IN-0) to 2010 °C (IN-20) (Fig. 2f). This change in the predicted liquidus temperature is consistent with the primary formation of refractory multicomponent carboborides and borides during solidification**.** Consequently, the Laves phase predicted to be suppressed: JMatPro diagrams at room temperature (Fig. 2e) show its volume fraction dropping from 5 vol% in the pure alloy to zero at 20 vol % ceramic filler.

These simulation results are corroborated by BSE-SEM observations (Fig. 5). In the IN-0 alloy, interdendritic zones are dominated by bright-contrast (Nb- and Mo-rich) skeletal Laves networks, whereas in the IN-20 composite, these regions are occupied by dark-contrast features attributed to an *in situ*-formed boride eutectic. Nb and Mo segregated into the final portion of liquid and may interact with rejected B and Cr, forming Nb-Cr-Mo-rich eutectic boride channels (Table 3, Fig. 10b). Although the measured boron content (Table 3) may be somewhat overestimated due to matrix effects affecting the EPMA analysis of this light element, the elevated levels are consistent with solute segregation to the final solidification fronts. The eutectic boride network thus appears to replace the native Laves skeleton, creating a rigid interdendritic structure that may affect the deformation response of the composite layer [55].

The high energy density of the laser beam promotes melting and redistribution of the elements in the NbC–TiC–TiB_2 precursor system. *In-situ* phase formation is governed by thermodynamic stability, expressed in terms of Gibbs free energy (ΔG), and by kinetic constraints on

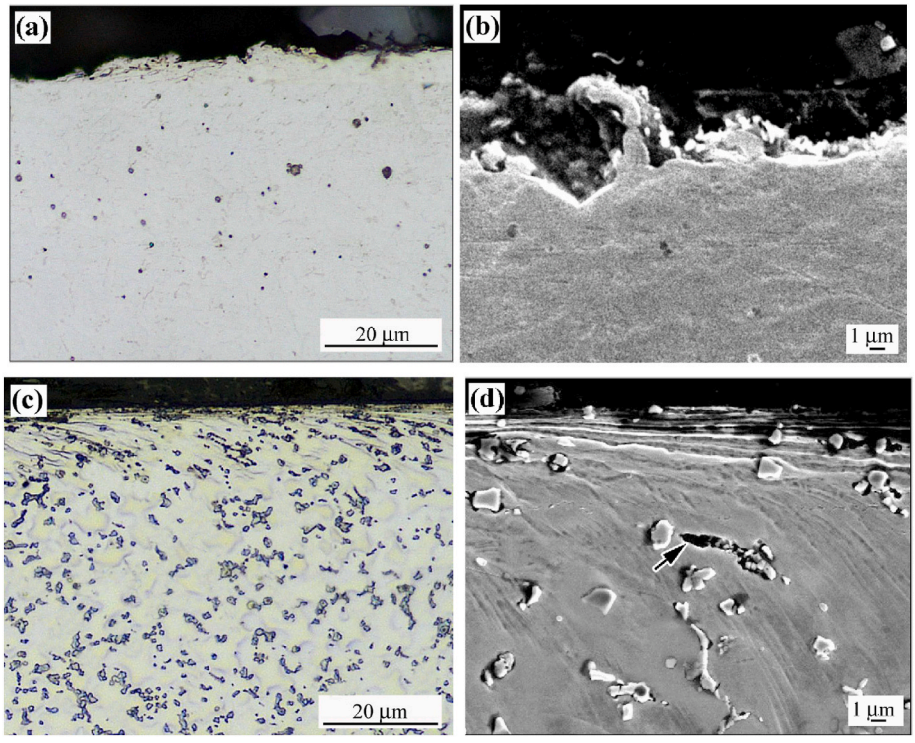

Fig. 16. Subsurface deformation and wear-induced damage within the wear track (longitudinal cross-section): (a, b) material pull-out in the IN-0 alloy and (c, d) subsurface-localized plastic deformation in the IN-20 composite, the latter representing a shallow-relief region of the wear track.

diffusion and nucleation during rapid solidification. The probability of forming specific phases in the alloys studied depends on variations in free energy, which are described by the equations given below (in kJ/mol) [56]:

$$\Delta G_f^0(Ni_2Nb) = -82.5 + 0.015 \cdot T, \quad (5)$$

$$\Delta G_f^0(NbC) = -130.0 + 0.002 \cdot T, \quad (6)$$

$$\Delta G_f^0(TiC) = -184.1 + 0.012 \cdot T, \quad (7)$$

$$\Delta G_T^0(TiB_2) = -279.5 + 0.014 \cdot T, \quad (8)$$

$$\Delta G_f^0(2/3Al_2O_3) = -1050.0 + 0.21 \cdot T, \quad (9)$$

$$\Delta G_f^0(TiO_2, rutile) = -944.7 + 0.18 \cdot T, \quad (10)$$

$$\Delta G_f^0(TiN) = -337.7 + 0.096 \cdot T. \quad (11)$$

From a thermodynamic standpoint, interstitial carbon and boron atoms exhibit a far higher chemical affinity for niobium than for nickel. The Gibbs free-energy functions of MC-type carbides (NbC, TiC) and borides are significantly more negative across the entire temperature range than that of the Laves phase (Ni_2Nb), as shown in Fig. 17. Consequently, the extra niobium from the precursor, together with native niobium segregated from solidifying γ-Ni dendrites, is largely consumed in the formation of a stable *in-situ* NbC-based multicomponent carboboride phase, described by the composition (Nb,Ti,Cr,Mo) (B,C) based on the elemental ratios reported in Table 3. This exhaustive partitioning leaves reduced the niobium content of the interdendritic liquid, thereby limiting the formation of the Laves phase during final solidification.

Microstructural analysis shows that rapid cooling drives the solidifying system away from equilibrium, resulting in equiaxed duplex carboboride inclusions and a multicomponent interdendritic eutectic. Laser surface melting in ambient air saturates the melt pool with atmospheric oxygen and nitrogen, which compete with solute carbon and boron for reaction with titanium. Titanium and aluminum exhibit strong thermodynamic affinities for oxygen, as indicated by the Gibbs free energies of formation their compounds (Fig. 17). The more negative formation energies of their oxides favor oxidation over the formation of carbides, nitrides, or borides. Titanium has a stronger thermodynamic affinity for oxygen than for nitrogen under the conditions considered, as the formation energy of TiN is less negative than those of the titanium oxides (Fig. 17). Strong Marangoni mixing and steep temperature gradients rapid interactions between the atmosphere and the molten alloy. Crystallization therefore may begin with complex Ti-Al-rich oxide inclusions that act as nucleation sites for the equiaxed duplex particles. The formation of such a complex oxide can be thermodynamically more favorable than the separate crystallization of titanium and aluminum oxides. As a representative example, the Al_2TiO_5 compound can be considered; its the standard Gibbs free energy of formation follows the temperature dependence [57]:

$$\Delta G_f^0(Al_2TiO_5) = -1965.0 + 0.394 \cdot T(\text{kJ/mol}) \quad (12)$$

As shown in Fig. 16, the thermodynamic stability of Al_2TiO_5 is predicted to significantly exceed that of individual TiO_2 or Al_2O_3 oxides, as well those of the carbides, nitrides, and borides considered, across the 1500-2500 K range. This energetic advantage may favor the preferential formation of the Ti–Al-rich oxide phase; consequently, complex Ti–Al–O cores may nucleate preferentially from the liquid phase (Fig. 18a). These particles may serve as heterogeneous nucleation substrates, lowering the activation energy barrier for the nucleation of subsequent phases, including the carboboride shell and γ-Ni matrix dendrites (Fig. 18b). As these phases grow, the remaining liquid is enriched with solute elements, leading to the crystallization of a multicomponent boride eutectic during the final stage of solidification (Fig. 18c). A similar nucleating effect of titanium oxide was documented in a study of dedicated to the laser processing of a multicomponent Fe-based W-Mo-V-Cr-Ti-C-B composite [29].

The origin of the weak nitrogen signal detected by EDS mapping in the spheroidal core requires careful consideration. This signal may arise from inherent limitations in the identification of low-energy X-ray peaks by EDS. In the ultra-soft X-ray range (below 1 keV), the N Kα line (≈392.4 eV) lies close to the Ti Lα series emission including a reported Ti L ℓ satellite line at ≈ 395 eV. Depending on the detector energy resolution and peak-processing procedure, these signals may be difficult to distinguish reliably. Consequently, the apparent nitrogen intensity spike may partly reflect the high local titanium concentration in the core. Therefore, although the incorporation of atmospheric nitrogen cannot be excluded, the available evidence is more compatible with a complex Ti–Al-O-type configuration than with a stoichiometric nitride.

A key microstructural feature of the hybrid SPS-LSM composites is the *in-situ* formation of equiaxed duplex precipitates with a well-defined core–shell architecture (Fig. 5g). To quantitatively evaluate the local solidification conditions, the primary dendrite arm spacing of the γ-Ni matrix was measured (Table 5). Using the empirically tailored Kurz–Fisher relation (Eq. (3)), effective local cooling rates ($\dot{T}$) were calculated for all alloy compositions. The *PDAS* shows a distinct non-monotonic N-shaped trend. At 5 vol% ceramics, *PDAS* decreases from 8.70 ± 0.40 μm (IN-0) to 4.91 ± 0.36 μm (IN-5), reflecting an increase in the estimated cooling rate from 1.72×10^3 K/s to 4.15×10^3 K/s. This refinement may result from the barrier effect of the initial *in-situ* precipitates, which restricted solute diffusion paths, and is consistent with numerical simulations of laser melting and cladding of superalloys [43,47,58]. In the IN-10 composition, the *PDAS* rises again to 5.73 ± 0.31 μm, with a corresponding decrease in the cooling rate to 3.24×10^3 K/s (Table 5). This transient deceleration may be associated with latent heat release during the crystallization of primary high-temperature carboboride inclusions. The resulting thermal effect may provide primary γ-Ni cells with additional time for diffusion-driven growth behind the solidification front. At the maximum reinforcement level (IN-20), the effects of the increased ceramic fraction appear to outweigh this potential thermal effect. The high volume fraction of *in-situ* carboboride clusters and interdendritic boride networks forms obstacles to γ-FCC matrix dendrite growth, reducing *PDAS* to 3.85 ± 0.32 μm and raising the estimated cooling rate to 5.99×10^3 K/s. The increased fraction of carboborides

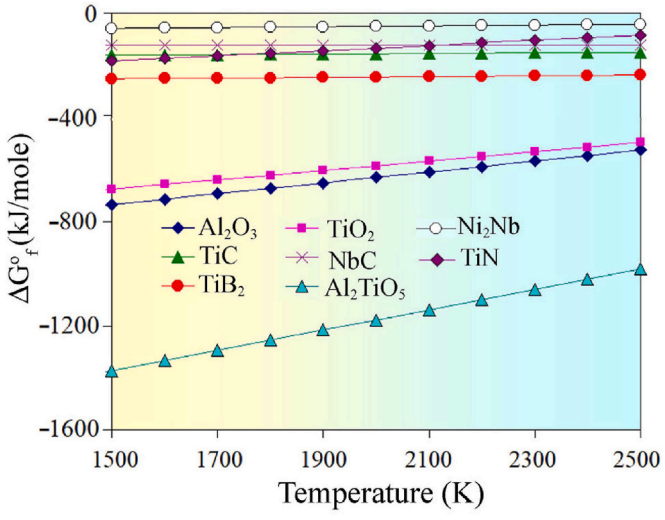

Fig. 17. Temperature dependence of the standard Gibbs free energy of formation (ΔG_f^0) for the potential oxide, carbide, nitride, and boride phases over the temperature range of 1500-2500 K.

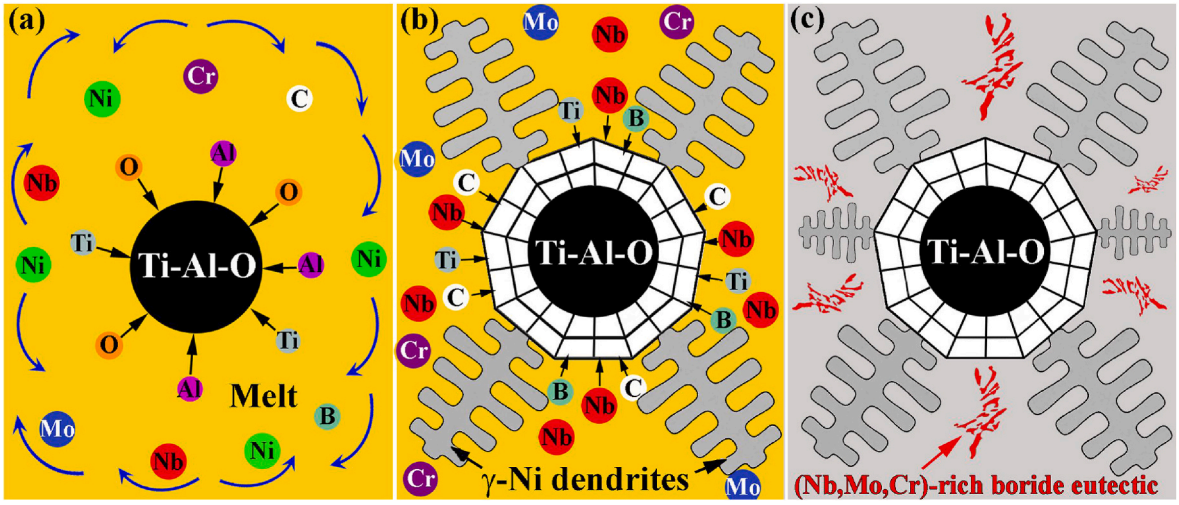

Fig. 18. Schematic illustration of the *in-situ* solidification and phase evolution sequence within the melt pool: (a) coupled interaction of liquid Ti, Al, and dissolved atmospheric oxygen driving the primary nucleation of the complex Ti–Al–O cores under convective Marangoni mixing; (b) heterogeneous growth of the faceted multicomponent carboboride shell on the oxide nuclei accompanied by the crystallization of primary γ-Ni dendrites; and (c) final solidification of a localized (Nb,Mo, Cr)-rich boride eutectic network within the residual melt.

Table 5
Quantitative microstructural parameters, calculated laser cooling rates (by Equation (3)), molten pool lifetimes, and atomic diffusion paths for the alloy configurations.

Alloy designation	Equilibrium solidification range, T_{liq}–T_{sol} (°C)	*PDAS* (μm)	Effective cooling rate, $\dot{T}$ (K/s)	Melt lifetime, t (s)	Light atoms (C, B, O, Al, Ti) path (μm)	Heavy atoms (Ni, Nb, Mo) path (μm)
IN-0	1350-1120	8.70 ± 0.40	1.72×10^3	0.134	36.60	23.20
IN-5	1420-1110	4.91 ± 0.36	4.15×10^3	0.084	29.20	18.40
IN-10	1680-1110	5.73 ± 0.31	3.24×10^3	0.176	42.00	26.50
IN-20	2010-1125	3.85 ± 0.32	5.99×10^3	0.148	38.50	24.40

may promote a transition from a unidirectional front to more multidirectional solidification, expanding the solidification-front area and potentially enhancing thermal dissipation. Furthermore, the addition of 20 vol% lightweight ceramic phases may alter the volumetric heat capacity of the melt relative to pure nickel, reducing its thermal inertia and potentially facilitating heat dissipation after the laser passes.

To assess the kinetic limitations of *in-situ* synthesis and solute redistribution, the molten-pool lifetime (t) and atomic diffusion distances (x) were evaluated using the calculated cooling rates. The melt lifetime was estimated from the solidification temperature intervals obtained from Scheil-Gulliver simulations (Table 5). Migration distances of the solute elements within the superheated laser melt pool were calculated using the classical diffusion length relationship [59]:

$$x = \sqrt{2D_{liquid} \cdot t}, \tag{13}$$

where D_{liquid} is the liquid-state diffusion coefficient, assumed to be 5×10^{-9} m^2/s for interstitial and light elements (C, B, O, Al, Ti) and 2×10^{-9} m^2/s for heavy substitutional matrix solutes (Ni, Nb, Mo) [60].

The calculations (Table 5) indicate that the heavy substitutional elements have diffusion distances of 18.4-26.5 μm during the transient melt lifetime (t = 0.084-0.176 s). These distances exceed the dendritic scale (*PDAS* = 3.85-8.70 μm), suggesting that diffusion over distances greater than the characteristic dendrite spacing is possible within the melt lifetime. Therefore, the heavy solutes are kinetically unconstrained and could theoretically segregate as isolated mono-component interdendritic phases. However, microstructural observations indicate that isolated homogeneous nucleation was not the dominant pathway; instead, the elements preferentially co-precipitated on pre-existing oxide surfaces, forming a coordinated duplex core-shell architecture. This observation suggests that shell formation during non-equilibrium solidification was governed not only by kinetics but also by interfacial thermodynamics, including the reduction of excess interfacial free energy.

As shown above, the crystallization begins with Ti–Al–O oxide inclusions, which form near the upper end of the liquidus range and act as primary endogenous substrates [61] for the subsequent crystallization of the high-Z, faceted Nb-rich carboboride shell. Shell formation can be described in terms of classical heterogeneous nucleation, using the interfacial geometric factor [62]:

$$\Delta G^*_{heterog.} = \Delta G^*_{\text{hom } og.} \cdot f(\theta), \tag{14}$$

$$f(\theta) = \frac{(2 + \cos\theta)\cdot(1 - \cos\theta)^2}{4}, \tag{15}$$

where θ is the contact angle between the nucleating carboboride phase and the solid oxide substrate; $f(\theta)$ is a geometric factor; $\Delta G^*_{heterog.}$ represents the critical Gibbs free energy barrier for the formation of a stable nucleus on a pre-existing solid substrate, and $\Delta G^*_{\text{hom } og.}$ denotes the corresponding energy barrier required for spontaneous, homogeneous nucleation in the bulk liquid melt.

This boundary configuration implies near-perfect reactive wetting ($\theta \to 0$, $\cos\theta \to 1$), for which the geometric factor $f(\theta)$ approaches zero. In high-energy molten pools, strong carbide-forming metals (Ti, Nb) may promote reactive wetting at oxide interfaces [63,64]. Chemisorption of these solutes at the oxide boundaries can lower the interfacial energy [65], while crystallographic coherence between the cubic carboboride lattice and the Ti–Al–O could further minimize lattice strain. SEM images show that carboborides formed a continuous encapsulating shell (Fig. 5g) rather than isolated particles typical of high wetting angles ($\theta > 90°$). In contrast to the poor wettability of pure nickel on conventional oxides, the Ti and Nb in the laser melt pool may segregate at oxide boundaries shifting the system toward a reactive wetting regime [66,

67]. This could reduces the solid–liquid interfacial energy and lower the effective wetting angle. Contact angles of approximately 5–10° have been reported for titanium-containing active-metal systems interacting with alumina [68]. Using θ = 5° in Equation (17) yields an extremely small shape factor $f(\theta) \approx 0.00001$. Under this assumption, the heterogeneous nucleation barrier ($\Delta G^*_{heterog.}$) would be by five orders of magnitude relative to homogeneous nucleation barrier ($\Delta G^*_{\text{hom } og.}$), potentially favouring nucleation at oxide interfaces over isolated carbide nucleation in the melt and promoting the formation of encapsulating carboboride shells.

Following the heterogeneous nucleation on the oxide surface, the subsequent overgrowth of the multicomponent shell is associated with the minimization of Gibbs free energy, which is expressed as:

$$\Delta G = \Delta H_{mix} - T \cdot \Delta S_{mix}, \tag{16}$$

where ΔH_{mix} and ΔS_{mix} represent the integral enthalpy of mixing and the configurational entropy of mixing, respectively.

To quantitatively evaluate the enthalpy of mixing, the extended semi-empirical Miedema framework [69] was applied using the following relationship proposed by Takeuchi and Inoue [70]:

$$\Delta H_{mix} = \sum 4 \Delta H^{mix}_{ij} c_i c_j, \tag{17}$$

where ΔH^{mix}_{ij} represents the characteristic enthalpy of mixing for each equiatomic binary system, and c_i and c_j denote the atomic fractions of the constituent elements obtained from the experimental data.

In the superheated laser melt pool, the broad mutual chemical solubility of the transition metals (Nb, Ti, Cr, Mo) and their chemical interactions with interstitials (C, B) can contribute substantial negative binary enthalpy terms. These attractive interactions dominate **may** outweigh positive contributions associated with electron-density mismatch, resulting in a strongly negative overall multicomponent ΔH_{mix} providing the thermodynamic energy needed to stabilize the carboboride shell and eutectic networks. The calculated ΔH_{mix} values are deeply negative: −67.5 kJ/mol for the carboboride shell and −36.2 kJ/mol for the eutectic borides.

To further assess the thermodynamic characteristics of the *in-situ* structures, the ideal configurational entropy of mixing (ΔS_{mix}) was also calculated using the multicomponent model based on the Compound Energy Formalism (CEF) introduced by Hillert [71] and applied to compositionally complex systems following Rost et al. [72]. Based on EDS data, the (Nb,Ti,Cr,Mo) (B,C) carboboride shell yields a calculated ΔS_{mix} value of 1.528R, reflecting the assumed atomic distribution across both metallic and interstitial sublattices. The *in-situ* eutectic phase exhibits a calculated ΔS_{mix} of 1.529R, based on the non-equimolar distribution of six transition metals (Cr, Nb, Ni, Mo, Fe, Ti) within its metallic sublattice (Table 3). The measured atomic proportion between the constituent boron (66.31 at.%) and the sum of transition metal constituents (33.69 at.%) in the newly formed eutectic phase are consistent with a 2:1 B-to-metal ratio, corresponding to the stoichiometry of an MB_2-type diboride. The formation of this phase may be favoured by strong covalent B–metal interactions, which can contribute to lowering the free energy of the residual melt [73,74]. Given the atomic ratios in Table 3 and the possibility that the detected nickel and iron partly result from matrix excitation during EDS analysis, the eutectic boride is represented as $(Cr,Nb,Mo,Ti)B_2$ for brevity.

According to the thermodynamic classification criteria for high-entropy ceramics (HECs) [19,75], the lower limit for ideal five-component high-entropy configurations is designated as $\Delta S_{mix} \geq 1.61R$ (R·ln(5)). Although structural constraints and non-equimolar partitioning within the *in-situ* phases may affect their configurational entropy, both calculated values (1.528R and 1.529R) significantly exceed the four-component threshold (1.38R) and closely approach the high-entropy boundary. This entropy-driven stabilization lowers the total Gibbs free energy during rapid laser solidification, suppressing the crystallization of coarse brittle intermetallics. The near-HEC nature of the *in-situ* phases may influence their mechanical and tribological behaviour through lattice distortion and diffusion kinetics [76,77]. Atomic size mismatch among Nb, Ti, Cr, and Mo within the carboboride sublattice may generate long-range strain fields that impede dislocation motion, contributing to high hardness and being consistent with the measured indentation hardness of 4.38 GPa, a 36% increase**.** The role of sluggish diffusion in preserving the eutectic and duplex architectures under frictional heating remains a possible mechanism to maintain load-bearing capacity during wear, consistent with the observed 58% reduction in wear rate.

The gradual transition from sharp crystallographic faceting to a corrugated, fringed outer morphology of the shell was observed as the precursor amount increased, becoming clearly pronounced in IN-20 (Fig. 5f). This is presumably associated with severe constitutional supercooling at the solidification front: at this maximum reinforcement level, high solute concentrations may promote morphological instability, disrupting planar layer-by-layer crystal growth [78]. Furthermore, shell growth occurs within the evolving microstructure alongside the advancing eutectic network**,** which may constrain the available growth space and contribute to an irregular, non-uniform morphology [79].

4.2. Quantitative morphometric phase evolution and micromechanical responses

An increase in the volume fraction of the ceramic precursor in the powder mixture was expected to increase the volume fraction of *in-situ* reinforcing inclusions within the composite structure. However, this trend was accompanied by particle coarsening [80], which became pronounced above a ceramic filler content of 5 vol% (Fig. 6b). The nonlinear coarsening behaviour was characterized by a 3.6-fold increase in the average size of the duplex core–shell particles, reaching 1.52 μm. This coarsening was associated with a widening of the solidification temperature interval (T_{Liq}–T_{Sol}) as the filler content increased (Fig. 2f).

To evaluate the kinetics of *in-situ* phase growth within the non-isothermal liquid melt pool, the parabolic growth model for an isolated spherical crystal growing from a supersaturated solution was applied according to the Frank analytical approach [81]:

$$r_{th} = 2\lambda\sqrt{D \cdot t}, \tag{18}$$

where r_{th} is the theoretical particle radius, t is the molten pool lifetime above the matrix solidus (0.148 s for the IN-20 sample according to Table 5), D is the diffusion coefficient of niobium in the melt, and λ is the dimensionless growth parameter.

Although the maximum diffusion coefficient estimated for heavy substitutional elements under convective mixing conditions in the superheated melt pool is 2×10^{-9} m^2/s (Table 5), an effective diffusion coefficient (D_{eff}) was used to account for continuous non-isothermal cooling when estimating the phase crystallization parameters. D_{eff} was calculated by integrating the Arrhenius equation over the entire crystallization temperature interval (2010-1125 °C), yielding 1.24×10^{-9} m^2/s.

Under moderate supersaturation conditions, the dimensionless growth parameter (λ) is defined using the Zener approximation [81]:

$$\lambda = \sqrt{S/2}, \tag{19}$$

where S is the dimensionless solute parameter characterizing the far-field supersaturation in the liquid phase.

The supersaturation parameter is expressed as follows:

$$S = \frac{C_\infty - C_e}{C_p - C_e}, \tag{20}$$

where C_∞ is the far-field solute concentration in the melt, taken as the

initial Nb concentration in the IN-20 specimen (10.45 wt%, Table 1), C_e is the equilibrium Nb solubility in liquid nickel (2.5 wt%), and C_p is the Nb concentration in the synthesized carbide phase (58.8 wt%, Table 3).

The calculated supersaturation parameter is $S = 0.141$, corresponding to a dimensionless growth parameter of $\lambda = 0.265$. Substituting these values into the Frank parabolic growth law yields a theoretical isolated particle radius of $r_{th} = 7.20$ μm. The difference between the calculated r_{th} and the experimentally measured average radius $r_{exp} = 0.76$ μm for IN-20 (Fig. 6b), may reflect limitations of the Frank model, which assumes unconstrained solute transport toward an isolated spherical particle. In contrast, multiple co-precipitating particles in the highly alloyed IN-20 melt may develop overlapping diffusion fields, promoting local solute depletion and limiting *in-situ* particle growth before solidification is complete.

This interpretation is consistent with observations of the interface between the carboboride particle and the matrix, obtained by high-magnification SEM/SEI imaging and quantitative EDS profiling across the γ-Ni matrix-particle transition zone (Fig. 19). The matrix–ceramic interface exhibits tight metallurgical bonding, with no evidence of microcracking or phase delamination (Fig. 19a). The quantitative elemental profile reveals a smooth compositional gradient across the phase boundary. Within the particle, the Nb content decreases from 46.7 wt% (point Spc_002) to 23.6 wt% (point Spc_005) at the interface, accompanied by an increase in Ni concentration from 4.8 wt% to 25.0 wt %. Beyond the interface, the EDS profile indicates a compositional gradient extending into the adjacent matrix (points Spc_006 and Spc_007), where the Nb content decreases from 3.9 wt% to 2.8%, falling below the detection limit only at point Spc_008.

This continuous elemental transition is consistent with the diffuse boundaries observed on the corresponding EDS maps (Fig. 19b). The resulting compositionally graded transition suggests good structural compatibility and metallurgical bonding between the *in-situ* synthesized phases and the Inconel 718 matrix. The formation of this gradient layer may be attributed to localized solute depletion at the rapid solidification front. As the growing carbide phase consumes Nb from the surrounding liquid, local Nb depletion may alter the crystallization pathway under extreme cooling conditions. Under substantial undercooling, Ni incorporation into peripheral lattice sites may sustain phase growth when Nb transport becomes rate-limiting.

This interpretation is consistent with the disappearance of unencapsulated oxide particles in compositions beyond IN-5, indicating a change in phase formation behaviour. At higher reinforcement levels (IN-10 and IN-20), the greater availability of Nb and Ti may favor shell growth around oxide particles over independent nucleation. This may promote the formation of core–shell structures around oxygen-rich cores.

The described changes in the size and number density of the *in-situ* inclusions were accompanied by changes in the micromechanical properties of the alloys. Specifically, the indentation hardness increased from 3.22 GPa (IN-0) to 4.38 GPa (IN-20; +36%), while the indentation modulus rose from 200.4 GPa to 228.7 GPa (+14%). Load–displacement curves show steeper slopes and reduced penetration depths, from approximately 2600 to 2250 nm, revealing increased contact stiffness. To evaluate the individual contributions of various metallurgical factors to the overall mechanical performance of the synthesized multicomponent composites, a quantitative strengthening model was applied. The total calculated yield strength (σ_y) of the modified layers is expressed using an additive superposition approach [82,83]:

$$\sigma_y = \sigma_0 + \sigma_{SS} + \sigma_{GB} + \sigma_{OR} + \sigma_{diss}, \tag{21}$$

where σ_0 is the lattice friction **stress** of pure nickel, taken as 20.0 MPa.

The solid-solution strengthening (σ_{SS}) of the FCC γ-Ni matrix is evaluated using the Fleischer relationship [84] based on the interaction parameter and lattice shear strains:

$$\sigma_{SS} = \sum 0.5 G \varepsilon_i^{3/2} c_i^{1/2} = \sum k_i \cdot C_i^{0.5}, \tag{22}$$

where G is the matrix shear modulus (76 GPa), ε is the solute-dislocation interaction parameter accounting for the size and modulus mismatch associated with the i-th element, and c_i is the atomic fraction of the solute. For practical engineering evaluation, the complex elastic interaction terms are represented by specific solute strengthening coefficients (k_i), calibrated directly against the weight concentrations (C_i, wt.%) determined by quantitative point EDS analysis of the matrix. The C_i coefficients are taken as 160, 110, 80 and 40 MPa·wt.%$^{-0.5}$ for Nb, Mo, Ti and Cr, respectively [84].

The strengthening contribution arising from solidification microstructure refinement is quantified via the classical Hall-Petch relationship:

$$\sigma_{H-P} = k_{H-P} \cdot d^{-0.5}, \tag{23}$$

where d is a characteristic structural parameter (taken as the experimentally determined *PDAS* values from Table 5 [85]), and k_{H-P} is the Hall-Petch parameter for Ni-based alloys, taken as 750 MPa μm$^{0.5}$ [86].

The resistance to dislocation glide provided by the incoherent *in-situ* phases and interdendritic secondary precipitates is evaluated using the modified Ashby-Orowan analytical expression [83]:

$$\sigma_{Or} = \frac{0.13 \cdot G \cdot b}{L} \cdot \ln\left(\frac{r_{exp}}{b}\right), \tag{24}$$

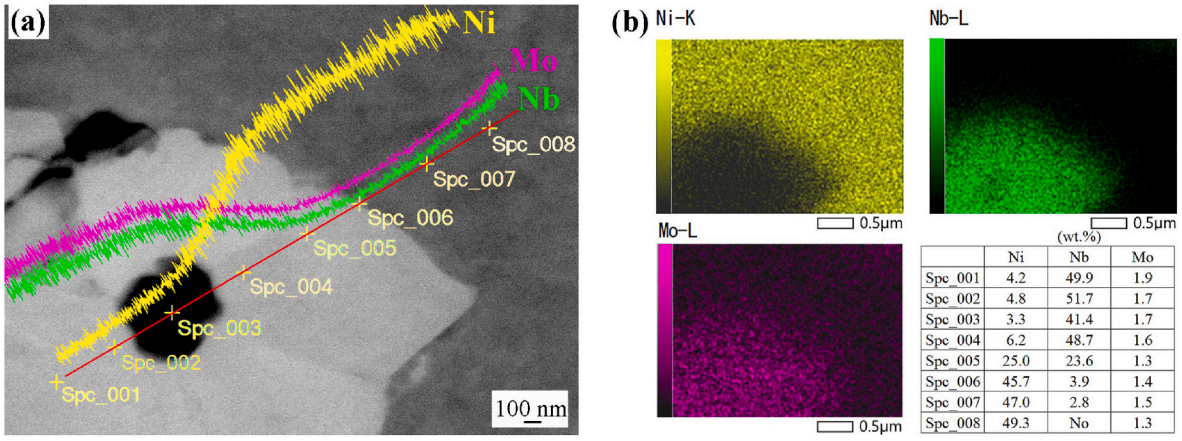

(wt.%)

	Ni	Nb	Mo
Spc_001	4.2	49.9	1.9
Spc_002	4.8	51.7	1.7
Spc_003	3.3	41.4	1.7
Spc_004	6.2	48.7	1.6
Spc_005	25.0	23.6	1.3
Spc_006	45.7	3.9	1.4
Spc_007	47.0	2.8	1.5
Spc_008	49.3	No	1.3

Fig. 19. Interfacial characterization of the in-situ synthesized duplex particle within the IN-20 sample: (a) high-magnification SEM/BSE micrograph showing the EDS line scan trajectory and elemental intensity profiles (Ni, Mo, Nb) across the particle-matrix boundary, and (b) corresponding EDS elemental maps of Ni, Nb, and Mo, along with a quantitative point-by-point composition table from points Spc_001 to Spc_008.

where G is the shear modulus (76 GPa for the Inconel 718 matrix), b is the Burgers vector (0.248 nm for the FCC nickel lattice), and r_{exp} is the average experimental particle radius, derived from the measured sizes of the monolithic and duplex phases for each specific composite (Fig. 6b). The parameter L denotes the mean interparticle spacing defined as [83]:

$$L = r_{exp} \cdot \left(\frac{2\pi}{3f}\right)^{0.5}, \quad (25)$$

where f represents the phase fraction (derived from Fig. 6a).

The dislocation forest strengthening (σ_{dis}) generated by the lattice defects is calculated using the Taylor dislocation model:

$$\sigma_{dis} = M \cdot \alpha \cdot G \cdot b \cdot \rho^{0.5}, \quad (26)$$

where M is the Taylor orientation factor (3.06 for FCC polycrystals), α is a geometric constant representing dislocation barrier efficiency (0.3), and ρ is the dislocation density (m^{-2}). The dislocation density values were estimated from the true full width at half maximum (FWHM, β) of the γ-Ni (111) X-ray diffraction peaks (Fig. 7) using the relationship [87]:

$$\rho = \frac{\beta^2}{9 \cdot b^2}. \quad (27)$$

The calculated strengthening contributions are presented in Table 6. The solid-solution strengthening contribution increases from 185.0 MPa (IN-0) to 230.5 MPa (IN-20), which is attributed to the progressive dissolution of the precursor constituents during laser processing. As the *PDAS* decreases from 8.70 μm in the IN-0 sample to 3.85 μm in the highly alloyed IN-20 composite, the Hall-Petch contribution rises from 254.4 MPa to 382.2 MPa, making it the substantial calculated strengthening contribution. X-ray diffraction analyses reveal a decrease in the FWHM values of the γ-Ni (111) peak from 0.36° (IN-0) to 0.23-0.27° for the ceramic-containing specimens. This decrease in peak broadening corresponds to a lower estimated dislocation density, from 7.1×10^{13} m^{-2} in IN-0 to $(2.9\text{-}4.0) \times 10^{13}$ m^{-2} in the composite variants, reducing the corresponding Taylor forest stress contribution from 146.0 MPa to 93.3-109.6 MPa. Overall, the Hall–Petch mechanism contributed 41.5-50.8% to the total composite strength. The inputs from solid-solution strengthening (30.2-32.1%) and dislocation forest strengthening (14.1-23.8%) are less significant, whereas the direct Orowan bowing contribution of the *in-situ* ceramic particles is marginal (under 2%) due to their relatively large size.

As the precursor content increases, the calculated yield strength gradually increases from 613.2 MPa to 752.2 MPa, exhibiting a strong correlation with the nanoindentation hardness profiles. The resulting hardness-to-yield strength ratio (Tabor factor, $C_{Tabor} = H_{exp}/\sigma_y$) ranges from 5.25 to 5.82. These values exceed the classical macroscale Tabor factor ($C_{Tabor} \approx 3.0$) which may be partly attributed to the indentation size effect associated with submicron Berkovich indentation [88]. Furthermore, the monotonic increase in the C_{Tabor} coefficient with a precursor content may reflect scale-dependent transition in deformation behaviour as the composite architecture becomes more heterogeneous. As the volume fraction of the *in-situ* high-modulus ceramic phases expands, they provide additional load support. The rigid particles constrain localized plastic flow and lateral extrusion of the surrounding γ-Ni matrix beneath the Berkovich tip, potentially contributing to the increase in the Tabor factor.

Table 6
Individual strengthening contributions (MPa) to the yield strength of the investigated compositions.

Strengthening Mechanism (Parameter)	IN-0	IN-5	IN-10	IN-20
Pure matrix lattice friction stress (σ_0)	20.0	20.0	20.0	20.0
Solid-solution (σ_{SS})	185.0	198.5	212.0	230.5
Hall-Petch refinement ($\sigma_{H\text{-}P}$)	254.4	285.1	321.4	382.2
Dispersion Orowan bowing contribution (σ_{Or})	7.8	12.2	13.7	9.5
Dislocation forest contribution (σ_{dis})	146.0	109.6	93.3	109.6
Total calculated yield strength (σ_y)	613.2	625.8	660.4	752.2
Experimental indentation hardness (H_{exp}), GPa	3.22	3.27	3.67	4.38
Resulting Tabor coefficient ($C = H_{exp}/\sigma_y$)	5.25	5.22	5.56	5.82

The elastoplastic behavior is characterized by energy-based indentation metrics: *ERI*, *PI*, and the h_p/h_{max} ratio (Fig. 11c). *ERI* values rise from 0.191 (IN-0) to a peak of 0.230 at 10 vol% ceramic content, indicating a greater stored elastic strain energy. At IN-20, *ERI* decreases to 0.211, whilr as *PI* increases to 0.789. This change may be associated with phase coarsening (up to 1.52 μm), which reduces the uniformity of interparticle spacing. The relatively stable h_p/h_{max} ratio (0.881-0.902) confirms that plastic deformation remains the dominant energy dissipation mechanism. Unlike embrittled conventional ex-situ composites, this *in-situ* formed phases and their interfaces may influence stress redistribution within the γ-Ni matrix, while dislocation motion along interdendritic regions may accommodate local deformation and limit stress accumulation.

4.3. Tribological behaviour

In addition to affecting micromechanical properties, the structural evolution associated with increasing ceramic content altered the composite tribological behavior. IN-0, IN-5, and IN-10 exhibit relatively uniform wear tracks with only minor width variations. In contrast, IN-20 shows pronounced periodic variations in track width and depth (Fig. 13a). This suggests a change in the wear mechanism that cannot be attributed solely to local interactions between the counterbody and individual carboboride particles. Based on the metallographic observations, cross-sectional analysis, and EDS data, the following wear mechanisms are proposed (Fig. 20).

In materials containing ≤10 vol% precursor, the tribological response was governed by severe adhesive interaction and delamination of oxide films. Their relatively low hardness allowed the surface to deform readily under contact with the WC ball, accomponied by the formation of brittle oxide films (Fig. 14a and c). Tensile stresses generated by tangential loading enhanced local pull-out of matrix material (Fig. 16a), followed by repeated detachment of oxide layers during sliding. The removal of oxide films, together with deformation-induced tensile zones in the subsurface regions, may facilitate oxygen penetration into the bulk material, thereby promoting internal oxidation rather than the formation of a compact and continuous protective surface oxide layer (Fig. 20a). This interpretation is supported by SEM observations, EDS line scans and elemental maps (Fig. 15a), which reveal significant oxygen enrichment beneath the residual oxide films on the worn surface. Repeated material removal and the oxide-film delamination contributed to increased wear rates and the formation of wear tracks with nearly constant cross-sectional profiles.

Unlike IN-0, IN-5, and IN-10, the IN-20 specimen exhibits pronounced periodic variations of wear-track width and depth (Fig. 13a). The characteristic modulation period is on the order of millimeters, far exceeding the size of individual carboboride particles. This suggests that the observed morphology is not controlled by local surface microgeometry but may be related to larger-scale processes involving the dynamic response of the tribometer-counterbody-specimen system. In the IN-20 composite, carboboride particles act as effective barriers to dislocation motion and restrict plastic flow in the matrix [89] (Fig. 16c). As a result, plastic deformation appears to be localized within a thin near-surface layer (Fig. 16d), producing significant strain hardening. The hardened layer may limit further deformation in the subsurface region and promotes localization of tribo-oxidation near the surface (Fig. 20b). This interpretation is consistent with the EDS results obtained from wear-track cross-sections (Fig. 16b), which show that oxygen is concentrated primarily within the surface tribolayer, while its content decreases rapidly with depth. Under such conditions, wear debris can

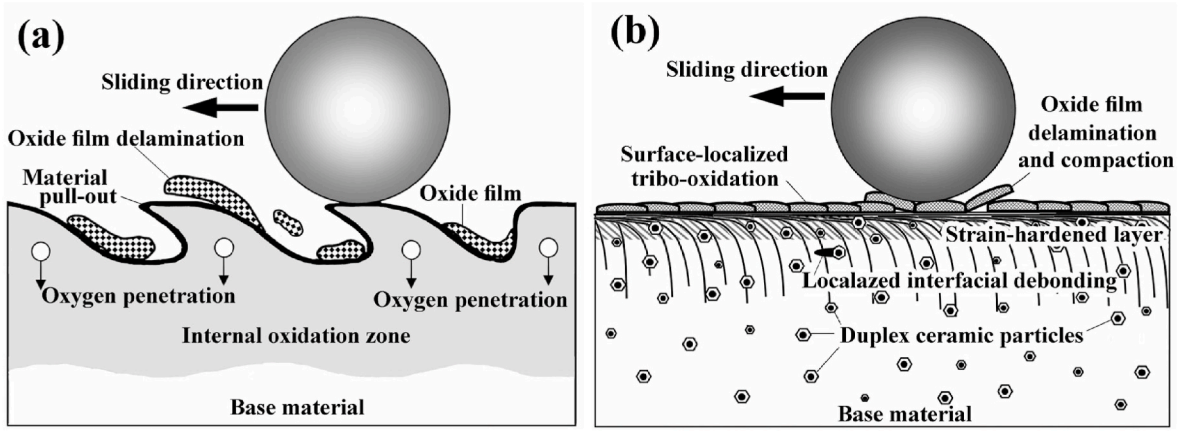

Fig. 20. Schematic comparison of the wear mechanisms operating in the investigated composites during sliding against a WC ball (longitudinal cross-sectional view): (a) IN-0 and (b) IN-20.

gradually accumulate, compact, and mechanically bond, leading to the formation of a dense tribolayer. At the same time, increasing ceramic content monotonically reduced the overall coefficient of friction from 0.95 (IN-0) to 0.77 for IN-20 (Fig. 12a). This reduction was likely driven by the carboboride skeleton mechanically shields the matrix from adhesive scuffing. The duplex particles contain Ti-oxide cores that may also influence interfacial friction [90], although their role as solid lubricants requires further experimental confirmation.

In IN-20, isolated microcracks are observed at the matrix–particle interface at a depth of approximately 10 μm (Fig. 16d), in regions of maximum bending of the fibrous deformation structure. However, the observed interfacial debonding remains localized and does not disrupt the continuity of the hardened surface layer. Furthermore, the lowest wear rate of IN-20 suggests that these microcracks are not the dominant wear mechanism but may instead represent a secondary consequence of localized plastic deformation within.

The addition of 20 vol% precursor not only strengthens the composite but also increases its elastic modulus by 14%. As a result, the surface layer becomes stiffer and less capable of dissipating mechanical energy through local plastic deformation. Consequently, a larger fraction of the input energy may be stored elastically and returned to the tribological system. It may therefore be hypothesized that, above a critical stiffness level, sliding-induced perturbations may trigger self-excited frictional oscillations in the tribometer-counterbody-specimen system. This interpretation is consistent with the pronounced fluctuations in the friction coefficient observed for IN-20 during both the running-in and steady-state stages of sliding (Fig. 12a). Such oscillations may lead to unstable contact conditions and periodic variations in normal load, producing cyclic changes in the local wear rate. Repetition of these cycles may result in the characteristic periodic modulation of wear-track width and depth observed in IN-20.

Overall, the experimental results suggest that the wear behaviour of IN-20 is governed not only by direct interaction between the counterbody and individual carboboride particles, but also by changes in the dynamic response of the tribological system associated with the increased composite stiffness. The proposed mechanism is consistent with the metallographic, EDS, and tribological observations. Nevertheless, further investigation of contact dynamics is needed to establish the origin of the distinct wear behaviour observed in the IN-20 composite.

5. Conclusions

Inconel 718-based composites containing 5-20 vol% of an NbC–TiC–TiB_2 precursor were fabricated by spark plasma sintering (SPS) followed by laser surface melting (LSM) in air. The combined processing route resulted in substantial changes in phase constitution, microstructure, indentation response, and wear behaviour. The main conclusions are as follows.

1. The combined SPS–LSM treatment resulted in the near-complete dissolution of the ceramic precursor during laser remelting, followed with the formation of equiaxed Ti–Al–O-rich oxide inclusions, which acted as substrates for the nucleation and growth of (Nb,Ti,Cr,Mo) (B,C) carboboride shells, producing a characteristic core–shell architecture. The remaining B- and Nb-containing constituents crystallized as an interdendritic eutectic network comprising multicomponent borides, including $(Cr,Nb,Mo,Ti)B_2$. Thermodynamic simulations predicted a decrease in the Laves-phase fraction with increasing precursor content, consistent with the observed evolution of the interdendritic structure.
2. Increasing the precursor content led to a monotonic rise in the area fractions of *in-situ* ceramic inclusions (equiaxed and eutectic) from 0.74% to 5.5% in IN-0 to 3.3% and 18.0% in IN-20, respectively. Concurrently, the average size of duplex inclusions increased more than threefold, from 0.42 to 1.52 μm, while their areal number density peaked at 0.089 μm^{-2} in IN-5 before falling to 0.036 μm^{-2} in IN-20, consistent with enhanced particle growth and agglomeration. From IN-10 to IN-20, the eutectic morphology transformed from thin, tortuous, high-BSE-contrast, Chinese-script-type plates to thicker, shorter plates with low BSE contrast.
3. The precursor content had a substantial effect on the micromechanical properties of the composites. The indentation hardness increased from 3.22 to 4.38 GPa (+36%), while the indentation modulus rose from 200.4 to 228.7 GPa (+14%) between IN-0 and IN-20. These changes are primarily attributed to the increasing fraction of hard *in-situ* carboborides and borides, which strengthen the matrix by impeding dislocation motion and contributing to load bearing, with dendritic refinement providing an additional contribution. The elastic recovery index reached a maximum of 0.230 in IN-10, whereas the h_p/h_{max} ratio remained within 0.881-0.902, indicating that plastic deformation remained dominant during indentation.
4. A progressive reduction in friction and wear was observed across the composite series. The steady-state coefficient of friction from 0.95 ± 0.11 in IN-0 to 0.77 ± 0.11 in IN-20 and lowered the wear rate from 2.31×10^{-4} to 0.97×10^{-4} $mm^3/(N{\cdot}m)$, corresponding to a 2.4-fold improvement in wear resistance. SEM and EDS analyses indicated differences in the dominant wear features: the unreinforced alloy exhibited extensive plastic deformation, oxide-film delamination, and oxygen enrichment beneath residual oxide films, whereas IN-20 showed shallow micro-ploughing grooves and a compacted surface tribolayer with oxygen concentrated near the surface. Periodic variations in wear-track width and depth, together

with pronounced friction fluctuations, were also observed in IN-20. These observations suggest the possible occurrence of oscillatory behavior in the tribological system, although this hypothesis requires further verification.

List of Abbreviations

BSE	Backscattered electrons
CEF	Compound Energy Formalism
CoF	Coefficient of friction
EDS	Energy-dispersive X-ray spectroscopy
EPMA	Electron probe microanalysis
ERI	Elastic recovery index
FCC	Face-centered cubic
HECs	High-entropy ceramics
IN718	Inconel 718 alloy (including IN-0, IN-5, IN-10, and IN-20 configurations)
LSM	Laser surface melting
LSW	Lifshitz–Slyozov–Wagner
MMCs	Metal matrix composites
OM	Optical microscopy
PDAS	Primary dendrite arm spacing
PI	Plasticity index
PMMCs	Particulate reinforced metal matrix composites
SEM	Scanning electron microscopy
SPS	Spark plasma sintering
TCP	Topologically close-packed phases (e.g., Laves phase)
XRD	X-ray diffraction

CRediT authorship contribution statement

Yu.G. Chabak: Writing – review & editing, Writing – original draft, Project administration, Investigation, Funding acquisition, Conceptualization. **V.G. Efremenko:** Writing – review & editing, Writing – original draft, Supervision, Resources, Methodology, Conceptualization. **N.P. Zaichuk:** Writing – review & editing, Writing – original draft, Methodology, Investigation, Conceptualization. **V. Puchý:** Investigation, Data curation. **B.V. Efremenko:** Software, Investigation, Formal analysis. **I. Petrišinec:** Visualization, Resources, Investigation. **K. Kamyshnykova:** Resources, Methodology, Investigation. **I.I. Sili:** Data curation, Investigation, Validation.

Declaration of competing interest

The authors declare that they have no known competing financial interests or personal relationships that could have appeared to influence the work reported in this paper.

Acknowledgements

This research was funded by the Slovak Research and Development Agency (APVV-24-0074). Efremenko B.V. and Sili I.I. acknowledge the financial support of the Ministry of Education and Science of Ukraine within the framework of project No. 0125U003128.

References

[1] Q. Huan, Review of Inconel 718: its history, properties, processing and developing substitutes, J. Mater. Eng. (2012) 92–100, https://doi.org/10.3969/j.issn.1001-4381.2013.06.001.

[2] G.H. Lee, B. Kim, J.B. Jeon, M. Park, S. Noh, B.J. Kim, Precipitate phase behavior and mechanical properties of Inconel 718 according to aging heat treatment time, Mater. Sci. Eng., A 924 (2025) 147776, https://doi.org/10.1016/j.msea.2024.147776.

[3] C. Slama, M. Abdellaoui, Precipitation kinetics of γ' and γ'' particles in Inconel 718 and its influence on mechanical properties, Mater. Today Commun. 38 (2024) 108158, https://doi.org/10.1016/j.mtcomm.2024.108158.

[4] Z. Xu, Z. Lu, J. Zhang, D. Li, J. Liu, C. Lin, The friction and wear behaviours of Inconel 718 superalloys at elevated temperature, Front. Mater. 8 (2021) 794701, https://doi.org/10.3389/fmats.2021.794701.

[5] P. Sun, N. Yan, S. Wei, D. Wang, W. Song, C. Tang, J. Yang, Z. Xu, Q. Hu, X. Zeng, Microstructural evolution and strengthening mechanisms of Inconel 718 alloy with different W addition fabricated by laser cladding, Mater. Sci. Eng., A 868 (2023) 144535, https://doi.org/10.1016/j.msea.2022.144535.

[6] I. Schramm Deschamps, D. dos Santos Avila, E. Vanzuita Piazera, R.C. Dudley Cruz, C. Aguilar, A.N. Klein, Design of in situ metal matrix composites produced by powder metallurgy – a critical review, Metals 12 (2022) 2073, https://doi.org/10.3390/met12122073.

[7] Y. Zhao, Z. Lu, L. Mi, Z. Hu, W. Yang, Morphological evolution of TiB_2 and $TiAl_3$ in Al–Ti–B master alloy using different Ti adding routes, Materials 15 (2022) 1984, https://doi.org/10.3390/ma15061984.

[8] Y. Cao, S. Zhi, H. Qi, Y. Zhang, C. Qin, S. Yang, Evolution behavior of ex-situ NbC and properties of Fe-based laser clad coating, Opt. Laser Technol. 124 (2020) 105999, https://doi.org/10.1016/j.optlastec.2019.105999.

[9] S. Zhang, G. Li, Y. Qu, H. Kang, Z. Chen, E. Guo, W. Zhang, T. Wang, Microstructure and mechanical properties of Cu–Cr–Zr–ZrB_2 composites by novel fabrication process of ultrasonic vibration treatment, J. Mater. Res. Technol. 31 (2024) 1461–1471, https://doi.org/10.1016/j.jmrt.2024.06.160.

[10] W. Wang, Y. Hui, Z. Jiang, Z. Hou, Z. Ye, J. Yang, S. Chen, J. Huang, In-situ reaction compositing behavior of the $Ni_{62}Ti_{38}$+C interlayer and its effects on interfacial microstructure and mechanical properties of the Cf/C-GH3044 joint, J. Mater. Res. Technol. 39 (2025) 1720–1731, https://doi.org/10.1016/j.jmrt.2025.09.208.

[11] X. Sun, X. Ren, W. Qiang, Y. Feng, X. Zhao, B. Huang, Microstructure and properties of Inconel 718 matrix composite coatings reinforced with submicron TiC particles prepared by laser cladding, Appl. Surf. Sci. 637 (2023) 157920, https://doi.org/10.1016/j.apsusc.2023.157920.

[12] G. Muvvala, S. Mullick, A.K. Nath, Development of process maps based on molten pool thermal history during laser cladding of Inconel 718/TiC metal matrix composite coatings, Surf. Coat. Technol. 399 (2020) 126100, https://doi.org/10.1016/j.surfcoat.2020.126100.

[13] R. Wang, D. Gu, H. Zhang, M. Guo, High temperature oxidation behavior of laser powder bed fusion printed WC/Inconel 718 composites, J. Mater. Sci. 57 (2022) 14119–14134, https://doi.org/10.1007/s10853-022-07520-1.

[14] W. Yang, W. He, Z. Hu, W. Duan, X. Ni, X. Deng, A. Wang, Y. Luo, F. Xie, Z. Chen, J. Liu, Z. Qu, F. Jin, L. He, Fabrication of Inconel 718 composites reinforced with TiCN via laser powder bed fusion: integration of triply periodic minimal surface lattice structures, J. Mater. Res. Technol. 32 (2024) 2443–2458, https://doi.org/10.1016/j.jmrt.2024.08.102.

[15] W. Wang, S. Wang, F. Chen, X. Zhang, Y. Xu, Microstructure and mechanical properties of TiN/Inconel 718 composites fabricated by selective laser melting, Acta Metall. Sin. 57 (2021) 1017–1026, https://doi.org/10.11900/0412.1961.2020.00485.

[16] R. Wang, W. Wang, G.L. Zhu, W.T. Pan, W.Z. Zhou, D.H. Wang, F. Li, H.J. Huang, Y.W. Jia, D.F. Du, A.P. Dong, D. Shu, B.D. Sun, Microstructure and mechanical properties of the TiN particles reinforced IN718C composite, J. Alloys Compd. 762 (2018) 237–245.

[17] B. Tang, Y. Tan, Z. Zhang, T. Xu, Z. Sun, X. Li, Effects of process parameters on geometrical characteristics, microstructure and tribological properties of TiB_2 reinforced Inconel 718 alloy composite coatings by laser cladding, Coatings 10 (2020) 76, https://doi.org/10.3390/coatings10010076.

[18] V.G. Khyzhniak, T.V. Loskutova, O.E. Datsyuk, I.S. Pohrebova, N.A. Kharchenko, T. P. Hovorun, A.I. Dehula, I.Y. Smokovich, Y.A. Kravchenko, High-entropy titanium–aluminum diffusion coatings on nickel alloy, High Temp. Mater. Process. 20 (2016) 267–278, https://doi.org/10.1615/HighTempMatProc.2017019326.

[19] G.M. Hingangavkar, High-entropy ceramics: from disorder to emerging functionalities, Ceram. Int. 51 (2025) 63519–63536, https://doi.org/10.1016/j.ceramint.2025.10.444.

[20] V. Kulyk, B. Vasyliv, Z. Duriagina, P. Lyutyy, V. Vavrukh, A. Kostryzhev, The effect of sintering temperature on phase-related peculiarities of the microstructure, flexural strength, and fracture toughness of fine-grained ZrO_2–Y_2O_3–Al_2O_3–CoO–CeO_2–Fe_2O_3 ceramics, Crystals 14 (2024) 175, https://doi.org/10.3390/cryst14020175.

[21] Ł. Rakoczy, M. Grudzień-Rakoczy, G. Cempura, T. Kargul, E. Rząd, M. Madej, T. Dudziak, D. Kozień, R. Cygan, R. Chulist, As-cast microstructure, wear and oxidation resistance of Alloy 718+TiC nanocomposites processed via suction casting, Ceram. Int. 52 (2026) 4669–4686, https://doi.org/10.1016/j.ceramint.2025.12.240.

[22] T. Ahmed, A. Mateen, S. Lee, Improved tribological performance and enhanced tensile adhesive strength of micro- to near-nanocrystalline WC-17 wt.% Co coatings sprayed using HVOF, Ceram. Int. 50 (2024) 11617–11624, https://doi.org/10.1016/j.ceramint.2024.01.064.

[23] Y.G. Chabak, V.I. Fedun, K. Shimizu, V.G. Efremenko, V.I. Zurnadzhy, Phase-structural composition of coating obtained by pulsed plasma treatment using eroded cathode of T1 high speed steel, Probl. At. Sci. Technol. 104 (2016) 100–106.

[24] A. Amanov, R. Karimbaev, C. Li, M.A. Wahab, Effect of surface modification technology on mechanical properties and dry fretting wear behavior of Inconel 718 alloy fabricated by laser powder-based direct energy deposition, Surf. Coat. Technol. 454 (2023) 129175, https://doi.org/10.1016/j.surfcoat.2022.129175.

[25] M.O. Vasylyev, B.M. Mordyuk, S.M. Voloshko, Surface post-processing of Inconel 718 alloy fabricated by additive manufacturing: selective laser melting, Prog. Phys. Met. 25 (2024) 614–642, https://doi.org/10.15407/ufm.25.03.614.

[26] J. Yang, F. Gao, Y. Tian, F. Dai, H. Zhang, Co-treatment of HIP and solution aging on microstructure evolution and high cycle fatigue properties of laser powder bed

melting Inconel 718, J. Alloys Compd. 1048 (2025) 184986, https://doi.org/10.1016/j.jallcom.2025.184986.
[27] S. Kusekar, S. Karki, A. Belure, S. Ahsan, D. Young, M. Grandhi, Z. Liu, T. Borkar, Comparative analysis of microstructure and mechanical properties of Inconel alloy 718 fabricated via laser powder bed fusion, laser metal deposition, and spark plasma sintering, Powder Technol. 483 (2026) 122863, https://doi.org/10.1016/j.powtec.2026.122863.
[28] Z.A. Duriagina, M.R. Romanyshyn, V.V. Kulyk, T.M. Kovbasiuk, A.M. Trostianchyn, I.A. Lemishka, The character of the structure formation of model alloys of the Fe-Cr-(Zr, Zr-B) system synthesized by powder metallurgy, J. Achiev. Mater. Manuf. Eng. 100 (2020) 49–57, https://doi.org/10.5604/01.3001.0014.3344.
[29] V.G. Efremenko, YuG. Chabak, I. Petrišinec, B.V. Efremenko, N.P. Zaichuk, T. M. Kovbasiuk, I.I. Sili, V. Puchý, A.G. Lekatou, In-situ carboboride-reinforced metal matrix composites via spark plasma sintering-laser surface melting hybrid processing: microstructure and wear behavior, J. Mater. Res. Technol. 42 (2026) 12209–12231, https://doi.org/10.1016/j.jmrt.2026.06.038.
[30] E. Tekoğlu, A.D. O'Brien, J.-S. Bae, K.-H. Lim, J. Liu, S. Kavak, Y. Zhang, S.Y. Kim, D. Ağaoğulları, W. Chen, A.J. Hart, G.-D. Sim, J. Li, Metal matrix composite with superior ductility at 800 ^{o}C: 3D printed In718+ZrB_2 by laser powder bed fusion, Compos. B Eng. 268 (2024), https://doi.org/10.1016/j.compositesb.2023.111052.
[31] G. Zhao, P. Zhang, J. Li, Z. Zhang, H. Li, L. Ma, Effects of different scanning speeds on microstructure evolution and tribological properties of Inconel 718 alloy vacuum electron beam surface modification, Mater. Today Sustain. 25 (2024) 100613, https://doi.org/10.1016/j.mtsust.2023.100613.
[32] V. Mandal, P. Tripathi, A. Kumar, S.S. Singh, J. Ramkumar, A study on selective laser melting (SLM) of TiC and B_4C reinforced IN718 metal matrix composites (MMCs), J. Alloys Compd. 901 (2022) 163527.
[33] Y. Kong, K. Peng, H. Huang, Additive manufacturing of high-strength Inconel 718 alloy through the addition of Ti_2AlC MAX particles, J. Mater. Sci. Technol. 158 (2023) 180–193, https://doi.org/10.1016/j.jmst.2023.01.059.
[34] W. Hu, Z. Huang, Q. Yu, Y. Wang, Y. Jiao, C. Lei, L. Cai, H. Zhai, Y. Zhou, Ti_2AlC triggered in-situ ultrafine TiC/Inconel 718 composites: microstructure and enhanced properties, J. Mater. Sci. Technol. 51 (2020) 70–78, https://doi.org/10.1016/j.jmst.2020.04.002.
[35] T. Zhang, J. Zhou, J. Wang, X. Meng, P. Li, S. Huang, H. Zhu, Effect of hybrid ultrasonic-electromagnetic field on cracks and microstructure of Inconel 718/60% WC composites coating fabricated by laser cladding, Ceram. Int. 48 (2022) 33901–33913, https://doi.org/10.1016/j.ceramint.2022.07.339.
[36] Y. Liu, W. Liu, H. Fan, Q. Zhang, Y. Ma, F. Wang, H. Zhang, Role of nano-TiC particles in enhancing the microstructure and wear resistance of IN718 superalloys fabricated by directed energy deposition, Ceram. Int. 51 (2025) 46933–46944, https://doi.org/10.1016/j.ceramint.2025.07.398.
[37] A. Naughton-Duszová, M. Hrubovčáková, M. Vojtko, D. Albov, D. Medveď, L. Ďakovská, L. Medvecky, P. Hvizdoš, T. Csanádi, Fracture strength of grains and grain boundaries in a dual-phase high-entropy ultra-high temperature ceramics, J. Eur. Ceram. Soc. 44 (2024) 5422–5431, https://doi.org/10.1016/j.jeurceramsoc.2024.01.034.
[38] W. Xu, B. Jia, X. Liu, L. Ji, H. Zhou, J. Chen, C. Sun, H. Li, Structural evolution and mechanical properties of multi-element (TiCrZrVNb)C high entropy ceramics films by multi-arc ion plating, Ceram. Int. 48 (2022) 19191–19197, https://doi.org/10.1016/j.ceramint.2022.03.211.
[39] Z. Zhang, Y. Dong, J. Song, Y. Lin, T. Li, Q. Sun, X. Zhang, P. Lin, X. You, Y. Su, L. Hu, Y. Zhang, High-temperature tribological behavior of typical self-mated ceramics (Al_2O_3/Si_3N_4/SiC) in atmosphere and water-oxygen environments, Tribol. Int. 214 (2026) 111358, https://doi.org/10.1016/j.triboint.2025.111358.
[40] H.O. Pierson, Handbook of refractory carbides and nitrides. Properties, Characteristics, Processing and Applications, William Andrew Inc., 1996.
[41] R.G. Munro, Material properties of titanium diboride, J. Res. Natl. Inst. Stand. Technol. 105 (2000) 709–720, https://doi.org/10.6028/jres.105.057.
[42] Ł. Rakoczy, M. Grudzień-Rakoczy, G. Cempura, T. Kargul, E. Rząd, M. Madej, A. Kruk, T. Dudziak, D. Kozień, R. Cygan, R. Chulist, D. Galusek, Microstructure, phase transformation temperatures and long-term stability of ex-situ Alloy 718 + TiB_2 metal-ceramic nanocomposites as a repair coatings for aerospace applications, Sci. Rep. 16 (2026) 95, https://doi.org/10.1038/s41598-025-29049-4.
[43] V.G. Efremenko, A.G. Lekatou, B.V. Efremenko, YuG. Chabak, I. Petryshynets, D. Margariti, S. Emmanouilidou, V. Puchy, Laser beam surface modification of additively manufactured Ni-based superalloy: correlations of microstructure and tribological/corrosion properties, J. Mater. Res. Technol. 35 (2025) 4390–4411, https://doi.org/10.1016/j.jmrt.2025.02.063.
[44] A.M. Okoro, S.S. Lephuthing, L. Rasiwela, P.A. Olubambi, Nondestructive measurement of the mechanical properties of graphene nanoplatelets reinforced nickel aluminium bronze composites, Heliyon 7 (2021) e07978, https://doi.org/10.1016/j.heliyon.2021.e07978.
[45] M. Walczak, W.J. Nowak, W. Okuniewski, D. Chocyk, Effect of adding molybdenum on microstructure, hardness, and corrosion resistance of an $AlCoCrFeNiMo_{0.25}$ high-entropy alloy, Materials 18 (2025) 4566, https://doi.org/10.3390/ma18194566.
[46] C. Zhong, V. Pandian, N. Pirch, A. Gasser, G. Phanikumar, Heat Treatment Design for IN718 by Laser Metal Deposition with High Deposition Rates — Modeling, Simulation and Experiments, SSRN, 2020, https://doi.org/10.2139/ssrn.3711240.
[47] H. Yin, S.D. Felicelli, Dendrite growth simulation during solidification in the LENS process, Acta Mater. 58 (2010) 1455–1465, https://doi.org/10.1016/j.actamat.2009.10.053.
[48] M. Storchak, I. Zakiev, V. Zakiev, A. Manokhin, Coatings strength evaluation of cutting inserts using advanced multi-pass scratch method, Measurement 191 (2022) 110745, https://doi.org/10.1016/j.measurement.2022.110745.
[49] J. García-Fernández, J. Salguero, J.M. Vázquez-Martínez, I. del Sol, M. Batista, Influence of laser surface texture orientation on the tribological behavior of the WC-Co/Ti6Al4V pair in dry and lubricated conditions, Wear 571 (2025) 205852, https://doi.org/10.1016/j.wear.2025.205852.
[50] I.M. Zakiev, G.A. Gogotsi, M. Storchak, V.I. Zakiev, Glass fracture during micro-scratching, Surfaces 3 (2020) 211–224, https://doi.org/10.3390/surfaces3020016.
[51] V.G. Efremenko, YuG. Chabak, K. Shimizu, M.A. Golinskyi, A.G. Lekatou, I. Petryshynets, B.V. Efremenko, H. Halfa, K. Kusumoto, V.I. Zurnadzhy, The novel hybrid concept on designing advanced multicomponent cast irons: effect of boron and titanium (thermodynamic modelling, microstructure and mechanical property evaluation), Mater. Charact. 197 (2023) 112691, https://doi.org/10.1016/j.matchar.2023.112691.
[52] J. Xie, R.N. Raoelison, Y. Zhang, Y. Liu, W. Shou, P.-E. Mazeran, N. Kang, M. Rachik, Mesoscopic segregation in H13 steel molten pool during laser remelting: a combined influence of Marangoni convection and oxidation, J. Mater. Process. Technol. 316 (2023) 117956, https://doi.org/10.1016/j.jmatprotec.2023.117956.
[53] E.A. Brener, D.E. Temkin, Melting of alloys along the inter-phase boundaries in eutectic and peritectic systems, Acta Mater. 55 (2007) 2785–2789, https://doi.org/10.1016/j.actamat.2006.12.016.
[54] L. Yan, F. Liou, Optimization of multi-materials in-flight melting in laser engineered net shaping (LENS) process, Int. Solid Freeform Fabr. Symp. (2014) 1052–1064.
[55] YuG. Chabak, K. Shimizu, V.G. Efremenko, M.A. Golinskyi, K. Kusumoto, V. I. Zurnadzhy, A.V. Efremenko, Microstructure and phase elemental distribution in high-boron multicomponent cast irons, Int. J. Miner. Metall. Mater. 29 (2022) 78–87, https://doi.org/10.1007/s12613-020-2135-8.
[56] NIST-JANAF thermochemical tables, in: fourth ed., in: M.W. Chase (Ed.), J. Phys. Chem. Ref. Data Monogr, vol. 9, 1998.
[57] M. Ilatovskaia, G. Savinykh, O. Fabrichnaya, Thermodynamic description of the Ti-Al-O system based on experimental data, J. Phase Equilib. Diffus. 38 (2017) 175–184, https://doi.org/10.1007/s11669-016-0509-4.
[58] R. Yan, Z. Liu, Numerical simulation and experimental prediction of the cladding layer based on the response surface method, Coatings 13 (2023) 845, https://doi.org/10.3390/coatings13050845.
[59] M.J. Sohrabi, H. Mirzadeh, Estimation of homogenisation time for superalloys based on a new diffusional model, Mater. Sci. Technol. 36 (2020) 380–384, https://doi.org/10.1080/02670836.2019.1706906.
[60] M. Walbrühl, A. Blomqvist, P.A. Korzhavyi, Atomic diffusion in liquid nickel: first-principles modeling, J. Chem. Phys. 148 (2018) 244503, https://doi.org/10.1063/1.5026348.
[61] B. Trembach, M. Krbata, B. Haibadulov, O. Iokhov, I. Tsebriuk, I. Pomohaiev, Y. Korobkov, L. Neduzha, Optimisation of elemental transfer efficiency in Fe-C-Cr-Ti-Cu hardfacing by self-shielded flux-cored wire: a synergistic Taguchi–ANOVA–FD–PCA–GRA approach, Eng 7 (2026) 139, https://doi.org/10.3390/eng7030139.
[62] D.A. Porter, K.E. Easterling, M.Y. Sherif, Phase Transformations in Metals and Alloys, CRC Press, 2009.
[63] N. Frage, N. Froumin, M.P. Dariel, Wetting of TiC by non-reactive liquid metals, Acta Mater. 50 (2002) 237–245, https://doi.org/10.1016/S1359-6454(01)00349-4.
[64] H. Hosokawa, K. Shimojima, A. Matsumoto, K. Kato, T. Matsuda, H. Matsubara, Wetting behavior for Ni on $(Ti_{0.95}Mo_{0.05})(C_{0.5}N_{0.5})$, $(Ti_{0.9}Nb_{0.1})(C_{0.5}N_{0.5})$ and $(Ti_{0.8}Nb_{0.1}Mo_{0.05})(C_{0.5}N_{0.5})$ substrates, Mater. Trans. (2013), https://doi.org/10.2320/matertrans.M2012351.
[65] M. Ksiazek, B. Mikulowski, M. Richert, Effect of Nb+Ti coating on the wetting behavior, interfacial microstructure, and mechanical properties of Al/Al_2O_3 joints, J. Mater. Sci. 45 (2010) 2194–2202, https://doi.org/10.1007/s10853-010-4214-0.
[66] N. Eustathopoulos, M.G. Nicholas, B. Drevet, Wettability at High Temperatures, Pergamon, Oxford, 1999.
[67] B.O. Trembach, Y.A. Silchenko, M.G. Sukov, N.B. Ratska, Z.A. Duriagina, I. V. Krasnoshapka, O.V. Kabatskyi, O.M. Rebrova, Development of a model of transition element factor of alloying elements of self-shielding flux-cored powder wire and optimization of its core filler composition, Mater. Sci. 59 (2024) 733–740, https://doi.org/10.1007/s11003-024-00834-2.
[68] R. Voytovych, F. Robaut, N. Eustathopoulos, The relation between wetting and interfacial chemistry in the CuAgTi/alumina system, Acta Mater. 54 (2006) 2205–2214, https://doi.org/10.1016/j.actamat.2005.11.048.
[69] A.R. Miedema, A.K. Niessen, F.R. de Boer, R. Boom, Cohesion in Metals: Transition Metal Alloys, North-Holland Physics Publishing, Amsterdam, 1988.
[70] A. Takeuchi, A. Inoue, Classification of bulk metallic glasses by atomic size difference, heat of mixing and period of constituent elements and its application to characterization of laser-clad layers, Mater. Trans. 46 (2005) 2817–2829.
[71] M. Hillert, The compound energy formalism, J. Alloys Compd. 320 (2001) 161–176, https://doi.org/10.1016/S0925-8388(00)01481-X.
[72] C.M. Rost, E. Sachet, T. Borman, A. Moballegh, E.C. Dickey, D. Hou, J.L. Jones, S. Curtarolo, J.-P. Maria, Entropy-stabilized oxides, Nat. Commun. 6 (2015) 8485, https://doi.org/10.1038/ncomms9485.
[73] P. Vajeeston, P. Ravindran, C. Ravi, R. Asokamani, Electronic structure, bonding, and ground-state properties of AlB_2-type transition-metal diborides, Phys. Rev. B 63 (2001) 045115, https://doi.org/10.1103/PhysRevB.63.045115.
[74] O.V. Sukhova, Formation of structure and properties of boron-rich Fe–B–C alloys alloyed with Cr, V, Nb or/and Mo, Metallofiz. Noveishie Tekhnol. 43 (2021) 355–365, https://doi.org/10.15407/mfint.43.03.0355.
[75] J. Zhang, J. Liang, H. Li, Y. Yang, D. Huo, C. Liu, A review of high-entropy ceramics preparation methods, properties in different application fields and their regulation

methods, J. Mater. Res. Technol. 32 (2024) 1083–1117, https://doi.org/10.1016/j.jmrt.2024.07.153.

[76] A. Naughton-Duszová, P. Švec, M. Hrubovčáková, O. Petruš, M. Vojtko, P. Hvizdoš, J. Dusza, Processing and microstructure development of reactive sintered (Ti-Zr-Nb-Hf-Ta)B_2 + (Ti-Zr-Nb-Hf-Ta)C high-entropy ceramics, J. Eur. Ceram. Soc. 45 (2025) 116872, https://doi.org/10.1016/j.jeurceramsoc.2024.116872.

[77] B.-Y. Ni, Y. Zhang, H.-Z. Li, L.-H. Zhang, M.-X. Wu, J.-F. Peng, W.-Y. Xie, M.-M. Yan, Y.-F. Chai, Research progress and application prospect of high entropy carbide and high entropy carbonitride ceramics, Ceram. Int. 51 (2025) 61414–61431, https://doi.org/10.1016/j.ceramint.2025.10.461.

[78] P.C. Bollada, P.K. Jimack, A.M. Mullis, Faceted and dendritic morphology change in alloy solidification, Comput. Mater. Sci. 144 (2018) 76–84, https://doi.org/10.1016/j.commatsci.2017.12.007.

[79] S. Gaddam, M.S.K.K.Y. Nartu, A. Chesetti, S.A. Mantri, R.S. Mishra, N.B. Dahotre, R. Banerjee, Hierarchical phase evolution during direct laser deposition of an in-situ Ni-NbC composite, Scr. Mater. 226 (2023) 115225, https://doi.org/10.1016/j.scriptamat.2022.115225.

[80] YuG. Chabak, V.G. Efremenko, Change of secondary-carbides' nanostate in 14.5% Cr cast iron at high-temperature heating, Metallofiz. Noveishie Tekhnol. 34 (2012) 1205–1220.

[81] Y. Song, B. Radhakrishnan, S. Gorti, R. Acharya, Precipitate growth kinetics under inhomogeneous concentration fields using a phase-field model, Phys. Rev. Mater. 5 (2021) 053401, https://doi.org/10.1103/PhysRevMaterials.5.053401.

[82] A.J. Goodfellow, E.I. Galindo-Nava, K.A. Christofidou, N.G. Jones, C.D. Boyer, T. L. Martin, P.A.J. Bagot, M.C. Hardy, H.J. Stone, The effect of phase chemistry on the extent of strengthening mechanisms in model Ni-Cr-Al-Ti-Mo based superalloys, Acta Mater. 153 (2018) 290–302, https://doi.org/10.1016/j.actamat.2018.04.064. A.J.

[83] E.I. Galindo-Nava, L.D. Connor, C.M.F. Rae, On the prediction of the yield stress of unimodal and multimodal γ′ nickel-base superalloys, Acta Mater. 98 (2015) 377–390, https://doi.org/10.1016/j.actamat.2015.07.048.

[84] Z. Li, Z. Wang, Z. Wang, Z. Qin, F. Liu, et al., Quantifying solid solution strengthening in nickel-based superalloys via high-throughput experiment and machine learning, Comput. Model. Eng. Sci. 135 (2) (2023) 1521–1538, https://doi.org/10.32604/cmes.2022.021639.

[85] S. Keerti, X. Yang, N. Hari Babu, A generic Hall-Petch relationship in metallic materials with varied grain morphology, Mater. Sci. Eng., A 943 (2025) 148764, https://doi.org/10.1016/j.msea.2025.148764.

[86] R. Kozar, A. Suzuki, W. Milligan, J. Schirra, M. Savage, T.M. Pollock, Strengthening mechanisms in polycrystalline multimodal nickel-base superalloys, Metall. Mater. Trans. A 40 (2009) 1588–1603.

[87] Y. Yan, J. Huang, L. Pan, B. Meng, Q. Wei, B. Yang, A comparative study of methods for calculating the dislocation density in GaN-on-Si epitaxial wafers, Micromachines 15 (2024) 954, https://doi.org/10.3390/mi15080954.

[88] W.D. Nix, H. Gao, Indentation size effects in crystalline materials: a law for strain gradient plasticity, J. Mech. Phys. Solid. 46 (1998) 411–425, https://doi.org/10.1016/S0022-5096(97)00086-0.

[89] V.G. Efremenko, K. Shimizu, A.P. Cheiliakh, T.V. Pastukhova, YuG. Chabak, K. Kusumoto, Abrasive resistance of metastable V–Cr–Mn–Ni spheroidal carbide cast irons using the factorial design method, Int. J. Miner. Metall. Mater. 23 (2016) 645–657, https://doi.org/10.1007/s12613-016-1277-1.

[90] A. Krishnamurthy, K.A. Razak, B.S. Halemani, A. Buradi, A. Afzal, C.A. Saleel, Performance enhancement in tribological properties of lubricants by dispersing TiO_2 nanoparticles, Mater. Today Proc. 47 (2021) 6180–6184, https://doi.org/10.1016/j.matpr.2021.05.083.